

Planning of *EM* Skins for Improved Quality-of-Service in Urban Areas

A. Benoni,⁽¹⁾ M. Salucci,⁽¹⁾ *Member, IEEE*, G. Oliveri,⁽¹⁾ *Senior Member, IEEE*, P. Rocca,⁽¹⁾⁽²⁾ *Senior Member, IEEE*, B. Li,⁽³⁾⁽⁴⁾ and A. Massa,⁽¹⁾⁽³⁾⁽⁵⁾ *Fellow, IEEE*

⁽¹⁾ *ELEDIA Research Center (ELEDIA@UniTN - University of Trento)*

DICAM - Department of Civil, Environmental, and Mechanical Engineering

Via Mesiano 77, 38123 Trento - Italy

E-mail: {arianna.benoni, marco.salucci, giacomo.oliveri, paolo.rocca, andrea.massa}@unitn.it

Website: www.eledia.org/eledia-unitn

⁽²⁾ *ELEDIA Research Center (ELEDIA@XIDIAN - Xidian University)*

P.O. Box 191, No.2 South Tabai Road, 710071 Xi'an, Shaanxi Province - China

E-mail: paolo.rocca@xidian.edu.cn

Website: www.eledia.org/eledia-xidian

⁽³⁾ *ELEDIA Research Center (ELEDIA@TSINGHUA - Tsinghua University)*

30 Shuangqing Rd, 100084 Haidian, Beijing - China

E-mail: {andrea.massa, libaozhu}@tsinghua.edu.cn

Website: www.eledia.org/eledia-tsinghua

⁽⁴⁾ *Beijing National Research Center for Information Science and Technology (BNRist) - Tsinghua University*

30 Shuangqing Road, 100084, Haidian, Beijing - China

E-mail: libaozhu@tsinghua.edu.cn

⁽⁵⁾ *ELEDIA Research Center (ELEDIA@UESTC - UESTC)*

School of Electronic Engineering, Chengdu 611731 - China

E-mail: andrea.massa@uestc.edu.cn

Website: www.eledia.org/eledia-uestc

This work has been submitted to the IEEE for possible publication. Copyright may be transferred without notice, after which this version may no longer be accessible.

Planning of *EM* Skins for Improved Quality-of-Service in Urban Areas

A. Benoni, M. Salucci, G. Oliveri, P. Rocca, B. Li, and A. Massa

Abstract

The optimal planning of electromagnetic skins (*EMS*s) installed on the building facades to enhance the received signal strength, thus the wireless coverage and/or the quality-of-service (*QoS*) in large-scale urban areas, is addressed. More specifically, a novel instance of the System-by-Design (*SbD*) paradigm is proposed towards the implementation of a smart electromagnetic environment (*SEME*) where low-cost passive static reflective skins are deployed to enhance the level of the power received within selected regions-of-interest (*RoIs*). Thanks to the *ad-hoc* customization of the *SbD* functional blocks, which includes the exploitation of a digital twin (*DT*) for the accurate yet fast assessment of the wireless coverage condition, effective solutions are yielded. Numerical results, dealing with real-world test-beds, are shown to assess the capabilities, the potentialities, and the current limitations of the proposed *EMS*s planning strategy.

Key words: Smart *EM* Environment (*SEME*), *EM* Skins (*EMS*s), System-by-Design (*SbD*), Genetic Algorithms (*GAs*), Global Optimization, Wireless Network Planning.

1 Introduction

The smart electromagnetic environment (*SEME*) is without any doubt a promising and revolutionizing concept for the design of future wireless communications systems [1]-[4]. It is based on the idea that the environment should be no more regarded as an uncontrollable impairment to the overall quality-of-service (*QoS*). Conversely, it should be exploited as a powerful “tool” to enable unprecedented manipulations of the complex electromagnetic (*EM*) phenomena for enhancing the overall coverage, the data throughput, and the *QoS* [3][4]. As a matter of fact, fitting ever-growing needs for ubiquitous connectivity and low latency/resiliency of forthcoming communication standards, also beyond the fifth-generation (*5G*) [5]-[9], will be possible only if the propagation scenario will play a fundamental role in counteracting the distortions, the delays, the losses, and the fading of the *EM* waves radiated by the base-stations (*BTSs*).

A first step towards this path is to address the synthesis of the *BTS* in an unconventional way by fitting user-defined requirements on the *QoS*, while bypassing the optimization of standard free-space line-of-sight (*LOS*) key performance indicators (*KPIs*) (e.g., gain, sidelobe level, and half-power beamwidth). Indeed, these latter do not take into account the presence of the environment as a stakeholder of the overall system performance [3][10]. Within this framework, the approach in [3] optimizes the *BTS* excitations by opportunistically exploiting the *EM* interactions with the surrounding obstacles to fulfil user-defined radiation masks.

Otherwise, many studies have been recently carried out on the possibility to improve the performance of a wireless communication system by using reconfigurable intelligent surfaces (*RISs*) [11]-[22]. Such a technology consists of engineered tunable reflecting/refracting metasurfaces [23]-[29] that adaptively generate anomalous reflection/transmission of the impinging *EM* waves coming from the *BTSs*. Therefore, *RISs* are exploited to redirect the scattered *EM* wave towards arbitrary directions, not compliant with the classical Snell’s laws, where the received power would be otherwise weak/insufficient to support a desired throughput and *QoS*.

The development of effective *RIS*-based solutions has benefited from the many similarities with the well-established theory of both reflectarrays (*RAs*) [30][31] and transmitarrays (*TAs*) [32]. As a matter of fact, the design of advanced metasurfaces with tunable magnitude/phase modulation has been performed by properly extending the *RAs/TAs* synthesis concepts in order to

take into account the presence of finite-size arrangements of sub-wavelengths metallic elements mounted on wall surfaces [12]. However, some unsolved challenges need to be still faced to make *RIS*s an attractive technology for large-scale urban deployments [13][17]. Indeed, new technological advancements are expected to enable the installation of *RIS*s in wide regions as well as conformal to irregular surfaces with cost-efficient manufacturing, installation, and maintenance, while consuming a low power. Moreover, new switching topologies and materials (e.g., graphene and liquid crystals) are under investigation to improve the sub-optimal performance of *PIN* diodes and varactors, which are currently employed to implement the *RIS* reconfigurability in sub-6GHz and millimeter wave/terahertz systems [13][29][32].

Static passive *EM* skins (*EMS*s) [4] are a promising simpler, lighter, and cheaper alternative to *RIS*s for increasing the wireless coverage and/or reducing the occurrence of “blind spots” in urban scenarios. *EMS*s leverage on the capabilities of passive modulated metasurfaces to control the *EM* interactions through a proper synthesis of their micro-scale physical structure [4]. The absence of diodes, varactors, phase shifters, amplifiers, and other components makes them particularly attractive for a low-cost deployment/maintenance in large-scale environments. However, while the facades of the buildings are strategic (e.g., no other costs for realizing customized supporting infrastructures) for the installation of *EMS*s, a suitable selection of the minimum number of buildings where the *EMS*s should be installed is mandatory to yield reliable as well as feasible solutions for recovering/yielding the desired *QoS* within specific regions-of-interest (*RoIs*).

Within this context, this paper addresses, for the first time to the best of the authors’ knowledge, the planning of *EMS*s in real-world urban scenarios. The proposed strategy is not customized to a specific technological implementation of the *EMS*s and it gives the wireless operator a full control of which “candidate” facades/buildings can be used to mount the *EMS*s. More specifically, the problem at hand is formulated as a global optimization one, which is efficiently solved within the System-by-Design (*SbD*) framework [33][34] to yield an optimal (i.e., max-coverage-improvement and lowest-cost) *EMS*s configuration that provides the desired level of received power within the *RoIs*. Towards this end, a proper selection, customization, and interconnection of the functional blocks of the *SbD* scheme is carried out starting from the definition

of a suitable binary representation of the solution space, which is then effectively explored with a customized implementation of the binary genetic algorithm (*BGA*) [35]-[38]. Moreover, a fast surrogate of the accurate, but time-consuming, ray-tracing (*RT*)-based *EM* coverage simulator is built according to the learning-by-examples (*LBE*) paradigm [39].

The paper is organized as follows. Section 2 describes the mathematical formulation of the problem at hand, while the *SbD*-based planning strategy is detailed in Sect. 3. Numerical results are then shown (Sect. 4) to assess the effectiveness and the potentialities as well as the current limitations of the proposed approach for the deployment of *EMS*s in real-world urban scenarios. Finally, some conclusions and final remarks are drawn (Sect. 5).

2 Mathematical Formulation

Let us consider a large-scale urban propagation scenario Ξ served by a *BTS* antenna located at the position \mathbf{r}_Ψ [$\mathbf{r}_\Psi = (x_\Psi, y_\Psi, z_\Psi)$] (Fig. 1) and working at the operating frequency f . Due to obstructions (caused by buildings/vegetation and other shadowing obstacles), reflections (due to reflective surfaces), refractions (owing to the presence of media characterized by different propagation velocities), and diffractions (generated by edges), the *EM* waves radiated by the *BTS* towards the mobile terminals propagate in non-line-of-sight (*NLOS*) conditions and multi-path phenomena arise. As a consequence, there is a set of S ($S \geq 1$) *RoIs*, $\underline{\Omega} = \{\Omega^{(s)}; s = 1, \dots, S\}$, within the urban scenario Ξ (Fig. 1) where the received power [40][41] turns out to be lower than the minimum coverage threshold, \mathcal{P}_{th} , which guarantees a target throughput and a suitable *QoS* to the end-users

$$\mathcal{P}_0(\mathbf{r}) < \mathcal{P}_{th} \quad \mathbf{r} \in \Omega^{(s)} \quad (s = 1, \dots, S). \quad (1)$$

In order to restore the wireless coverage condition ($\mathcal{P}(\mathbf{r}) \geq \mathcal{P}_{th}$) within the area Ξ served by the *BTS*, a set of *EMS*s is deployed to reflect an adequate level of power towards each s -th ($s = 1, \dots, S$) *RoI* $\Omega^{(s)}$. It is worth pointing out that the introduction of such field manipulation devices to implement a *SEME* cannot be arbitrary since *EMS*s can be mounted only on the facades of the buildings by also taking into account the architectural constraints. Moreover,

the number of *EMSs* must be kept as low as possible to reduce the overall cost as well as to minimize the environmental impact.

Owing to the “feasibility” constraint, a set of $W^{(s)}$ “candidate” building walls, $\underline{\tau}^{(s)} = \{\tau_w^{(s)}; w = 1, \dots, W^{(s)}\}$, in the neighborhood of each s -th ($s = 1, \dots, S$) *RoI* $\Omega^{(s)}, \Pi^{(s)}$ (Fig. 2), is selected for the installation of *EMSs* by the network operator. Thus, there are K ($K = \sum_{s=1}^S W^{(s)}$) admissible locations for deploying the *EMSs* in the urban scenario at hand. Accordingly, the *EMSs* planning problem can be stated as follows

Optimal *EMSs* Planning Problem (*OPP*) - Given K admissible sites, determine the locations and the layouts of the minimum number Q ($Q \ll K$) of *EMSs* so that the power $\mathcal{P}(\mathbf{r})$ received within the s -th ($s = 1, \dots, S$) *RoI* ($\mathbf{r} \in \Omega^{(s)}$) fulfils the coverage/*QoS* condition $\mathcal{P}(\mathbf{r}) \geq \mathcal{P}_{th}$.

To solve such an *OPP*, an innovative instance of the *SbD* strategy is applied (Sect. 3).

3 *SbD* Solution Approach

Within the *SbD* framework [3], the *EMSs* planning is carried out by implementing the following *SbD* blocks (Fig. 3):

1. *EMSs Design (EMSD - Sect. 3.1)* - The purpose of this block is the synthesis of the complete set $\underline{\Gamma}$ of K “admissible” *EMSs*, $\underline{\Gamma} = \{\Gamma_w^{(s)}; w = 1, \dots, W^{(s)}; s = 1, \dots, S\}$, starting from the knowledge of the locations of the *BTS*, \mathbf{r}_{Ψ} , of the selected *RoIs*, $\{\mathbf{r}_{\Omega}^{(s)}; s = 1, \dots, S\}$, and of the *EMSs* barycenters, $\{\mathbf{r}_w^{(s)}; w = 1, \dots, W^{(s)}; s = 1, \dots, S\}$, on the “candidate” building walls ($\mathbf{r}_w^{(s)} \in \tau_w^{(s)}$);
2. *Problem Formulation (PF - Sect. 3.2)* - This block implements two different tasks. On the one hand, it defines the set of U degrees-of-freedom (*DoFs*) to yield the most suitable encoding of the *OPP* unknowns, $\underline{\chi} = \{\chi_u; u = 1, \dots, U\}$. On the other hand, it mathematically formulates the *OPP* as a global optimization problem by defining a fitness function, $\varphi\{\underline{\chi}\}$, that measures the mismatch between the *OPP* objectives and the *EMSs* configuration coded by the *DoF* vector $\underline{\chi}$;

3. *Fitness Function Evaluation (FFE - Sect. 3.3)* - This block is aimed at efficiently evaluating the fitness associated to each trial solution, $\underline{\chi}$, of the *OPP*. To reduce the heavy computational load of a full-wave *EM* prediction of the wireless coverage within the *S RoIs* for any trial deployment of the *EMSs*, a fast yet reliable digital twin (*DT*) is exploited to assess the coverage condition in quasi real-time;
4. *Solution Space Exploration (SSE - 3.4)* - This block performs an effective sampling of the *U*-dimensional solution space to find the global optimum solution, $\underline{\chi}^{(opt)}$, that fulfils the project requirements by maximizing the fitness function $\varphi\{\underline{\chi}\}$ (i.e., $\underline{\chi}^{(opt)} = \arg\left[\max_{\underline{\chi}} \varphi\{\underline{\chi}\}\right]$). On the one hand, the implementation of the *SSE* block is based on the identification of the most effective optimization “engine” to deal with the *OPP-DoFs* defined by the *PF* block. On the other hand, it leverages on the fast predictions of the received power level generated by the *FFE* block to determine $\underline{\chi}^{(opt)}$ with a non-negligible time saving with respect to a standard integration of a full-wave *EM* solver within an optimization tool.

In the following, a detailed description of each *SbD* functional block is provided.

3.1 EMSD Block

Let us consider the design of the (w, s) -th ($w = 1, \dots, W^{(s)}$, $s = 1, \dots, S$) *EMS*, $\Gamma_w^{(s)}$, to be mounted on the building facade $\tau_w^{(s)}$ at the position $\mathbf{r}_w^{(s)}$ [$\mathbf{r}_w^{(s)} = (x_w^{(s)}, y_w^{(s)}, z_w^{(s)})$ - Fig. 4] for enhancing the strength of the signal received at the s -th *RoI*, $\Omega^{(s)}$, centered at $\mathbf{r}_\Omega^{(s)}$ [$\mathbf{r}_\Omega^{(s)} = (x_\Omega^{(s)}, y_\Omega^{(s)}, z_\Omega^{(s)})$ - Fig. 4]. Without loss of generality and by assuming a local coordinate system (x', y', z') with origin in $\mathbf{r}_w^{(s)}$ (Fig. 4), the *EM* wave radiated by the *BTS* towards $\Gamma_w^{(s)}$ is modeled as a monochromatic plane wave at frequency f with incident wave vector equal to

$$\mathbf{k}_\Psi^{(w,s)} = -\frac{2\pi}{\lambda} \left[\sin\left(\theta_\Psi^{(w,s)}\right) \cos\left(\varphi_\Psi^{(w,s)}\right) + \sin\left(\theta_\Psi^{(w,s)}\right) \sin\left(\varphi_\Psi^{(w,s)}\right) + \cos\left(\theta_\Psi^{(w,s)}\right) \right] \quad (2)$$

where $\theta_\Psi^{(w,s)}$ and $\varphi_\Psi^{(w,s)}$ are the elevation and the azimuth coordinates of the angle of incidence, respectively, whose expressions are

$$\begin{cases} \theta_{\Psi}^{(w,s)} = \mathcal{F}_{\theta}(\mathbf{r}'_{\Psi}) \\ \varphi_{\Psi}^{(w,s)} = \mathcal{F}_{\varphi}(\mathbf{r}'_{\Psi}), \end{cases} \quad (3)$$

$\mathcal{F}_{\theta}(\mathbf{r})$ and $\mathcal{F}_{\varphi}(\mathbf{r})$ being the Cartesian-to-Polar operators equal to

$$\begin{cases} \mathcal{F}_{\theta}(\mathbf{r}) = \arccos\left(\frac{z}{\sqrt{x^2+y^2+z^2}}\right) \\ \mathcal{F}_{\varphi}(\mathbf{r}) = \arctan\left(\frac{y}{x}\right). \end{cases} \quad (4)$$

Moreover, $\mathbf{r}'_{\Psi} [\mathbf{r}'_{\Psi} = (x'_{\Psi}, y'_{\Psi}, z'_{\Psi})]$ denotes the position of the *BTS* as seen from the *EMS* $\Gamma_w^{(s)}$ (Fig. 4) and its Cartesian coordinates are

$$\begin{cases} x'_{\Psi} = \mathcal{G}_x(\mathbf{r}_{\Psi}, \mathbf{r}_w^{(s)}) \\ y'_{\Psi} = \mathcal{G}_y(\mathbf{r}_{\Psi}, \mathbf{r}_w^{(s)}) \\ z'_{\Psi} = \mathcal{G}_z(\mathbf{r}_{\Psi}, \mathbf{r}_w^{(s)}) \end{cases}, \quad (5)$$

\mathcal{G}_c being the c -th ($c = x, y, z$) transformation operator defined as

$$\begin{cases} \mathcal{G}_x(\mathbf{r}, \mathbf{r}_w^{(s)}) = (x - x_w^{(s)}) \cos(\alpha_w^{(s)}) + (y - y_w^{(s)}) \sin(\alpha_w^{(s)}) \\ \mathcal{G}_y(\mathbf{r}, \mathbf{r}_w^{(s)}) = (z - z_w^{(s)}) \\ \mathcal{G}_z(\mathbf{r}, \mathbf{r}_w^{(s)}) = (x - x_w^{(s)}) \sin(\alpha_w^{(s)}) - (y - y_w^{(s)}) \cos(\alpha_w^{(s)}) \end{cases} \quad (6)$$

where $\alpha_w^{(s)}$ is the orientation angle of the building wall $\tau_w^{(s)}$ with respect to the global x -axis (Fig. 4).

Analogously, the angular direction of the *EM* wave reflected from the *EMS* $\Gamma_w^{(s)}$ towards the barycenter of $\Omega^{(s)}$, $(\theta_{\Omega}^{(w,s)}, \varphi_{\Omega}^{(w,s)})$, turns out to be

$$\begin{cases} \theta_{\Omega}^{(w,s)} = \mathcal{F}_{\theta}(\mathbf{r}_{\Omega}^{(s)'}) \\ \varphi_{\Omega}^{(w,s)} = \mathcal{F}_{\varphi}(\mathbf{r}_{\Omega}^{(s)'}) \end{cases} \quad (7)$$

$\mathbf{r}_{\Omega}^{(s)'} = \{\mathcal{G}_x(\mathbf{r}_{\Omega}^{(s)}, \mathbf{r}_w^{(s)}), \mathcal{G}_y(\mathbf{r}_{\Omega}^{(s)}, \mathbf{r}_w^{(s)}), \mathcal{G}_z(\mathbf{r}_{\Omega}^{(s)}, \mathbf{r}_w^{(s)})\}$ being the position of $\Omega^{(s)}$ in the *EMS* local system of coordinates (Fig 4).

Once the directions of incidence, $(\theta_{\Psi}^{(w,s)}, \varphi_{\Psi}^{(w,s)})$, and of reflection, $(\theta_{\Omega}^{(w,s)}, \varphi_{\Omega}^{(w,s)})$, of the impinging wave from the *BTS* are defined, the *EMS* $\Gamma_w^{(s)}$ ($w = 1, \dots, W^{(s)}$, $s = 1, \dots, S$) is designed according to the two-step synthesis procedure described in [4]. Shortly, the “reference” electric/magnetic current distributions on the surface of $\Gamma_w^{(s)}$, which radiate in far-field a pencil beam pointed towards the *RoI*, $(\theta_{\Omega}^{(w,s)}, \varphi_{\Omega}^{(w,s)})$, are computed. Then, the pattern of the metallizations [4] that compose the (w, s) -th ($w = 1, \dots, W^{(s)}$; $s = 1, \dots, S$) *EMS*, $\Gamma_w^{(s)}$, which is realized in low-cost *PCB* technology, is derived by optimizing the O geometric descriptors of the L unit cells of the *EMS*, $\underline{d}_w^{(s)} = \{d_{w,ol}^{(s)}; o = 1, \dots, O; l = 1, \dots, L\}$, so that the electric/magnetic current distributions induced on the surface $\Gamma_w^{(s)}$ by the impinging wave from the *BTS* match the “reference” ones.

3.2 PF Block

According to the *SbD* paradigm [3], the *PF* block is aimed at formulating the *OPP* into a proper mathematical framework to enable its reliable and cost-effective solution. Towards this end and owing to the problem at hand, a *binary encoding* is adopted to define the set of U *DoFs*. More in detail, a deployment of *EMSs* in the urban scenario is coded with the K -size (i.e., $U = K$) binary chromosome $\underline{\chi} = \{\chi_w^{(s)}; w = 1, \dots, W^{(s)}; s = 1, \dots, S\}$ whose (w, s) -th ($w = 1, \dots, W^{(s)}$, $s = 1, \dots, S$) entry is equal to 0 / 1 ($\chi_w^{(s)} = 1/\chi_w^{(s)} = 0$) when the (w, s) -th *EMS*, $\Gamma_w^{(s)}$, designed in the *EMSD* block (Sect. 3.1), is installed/not-installed on the corresponding building facade $\tau_w^{(s)}$.⁽¹⁾

The arising binary-coded planning problem is then formulated by the *PF* block as a global optimization task by properly defining the fitness function φ . Such a performance index mathematically models the underlying physics by quantifying the fulfilment of the *QoS* requirement by a trial solution $\underline{\chi}$ (i.e., a trial *EMSs* deployment). More specifically, the fitness of a guess $\underline{\chi}$, $\varphi\{\underline{\chi}\}$, is given by the inverse of a two-term single-objective cost function $\Phi\{\underline{\chi}\}$ ($\varphi\{\underline{\chi}\} \triangleq \frac{1}{\Phi\{\underline{\chi}\}}$)

$$\Phi\{\underline{\chi}\} = \Phi_{cov}\{\underline{\chi}\} + \Phi_{cost}\{\underline{\chi}\}. \quad (8)$$

⁽¹⁾For the sake of notation conciseness, the following notation will be also used in the description of the optimization strategy: $\underline{\chi} = \{\chi_k; k = 1, \dots, K\}$, $\chi_k = \{0, 1\}$ when the k -th *EMS*, Γ_k , is installed/not-installed on the k -th building facade, τ_k .

The *coverage term* $\Phi_{cov} \{\underline{\chi}\}$ measures the mismatch between the power received within the S *RoIs* and the threshold value \mathcal{P}_{th} through the following expression

$$\Phi_{cov} \{\underline{\chi}\} \triangleq \frac{1}{M} \sum_{s=1}^S \sum_{m=1}^{M^{(s)}} \frac{|\mathcal{P}_{th} - \mathcal{P}(\mathbf{r}_m^{(s)} | \underline{\chi})|}{|\mathcal{P}_{th}|} \mathcal{H} \{\mathcal{P}_{th} - \mathcal{P}(\mathbf{r}_m^{(s)} | \underline{\chi})\} \quad (9)$$

where $M^{(s)}$ is the number of receivers that lay in the positions, $\{\mathbf{r}_m^{(s)}; m = 1, \dots, M^{(s)}\}$ [$\mathbf{r}_m^{(s)} = (x_m^{(s)}, y_m^{(s)}, h)$], of the s -th ($s = 1, \dots, S$) *RoI* at a height h above the ground level (i.e., $z = 0$ - Fig. 1), $M = \sum_{s=1}^S M^{(s)}$, and \mathcal{H} is the Heaviside function (i.e., $\mathcal{H}\{a\} = 1$ if $a > 0$ and $\mathcal{H}\{a\} = 0$, otherwise).

The second term in (8) is proportional to the number of deployed *EMSs* and it is defined as follows

$$\Phi_{cost} \{\underline{\chi}\} \triangleq \frac{Q}{K}, \quad (10)$$

Q being equal to the ℓ_0 -norm of $\underline{\chi}$, $Q = \|\underline{\chi}\|_0$.

The fittest solution of the *OPP*, $\underline{\chi}^{(opt)}$, is the global minimum of (8)

$$\underline{\chi}^{(opt)} = \arg \left[\min_{\underline{\chi}} \Phi \{\underline{\chi}\} \right], \quad (11)$$

that is the best trade-off between the maximum power received in the *RoIs* and the minimum number of installed *EMSs*. Indeed, the presence of a larger number of *EMSs* generally would imply a greater level of power in the *RoIs* ($\Phi_{cov} \{\underline{\chi}\} \downarrow$), but at the cost of a higher implementation cost and a heavier wireless network complexity as well as a bigger architectural/environmental impact ($\Phi_{cost} \{\underline{\chi}\} \uparrow$).

3.3 FFE Block

The computation of the fitness of each trial solution $\underline{\chi}$, $\varphi \{\underline{\chi}\}$, could represent the main bottleneck of the overall *OPP* solution strategy, especially if repeated many times as in the *SSE* block for the exploration of the K -dimensional solution space (Sect. 3.4), unless suitable countermeasures are undertaken. As a matter of fact, even though the evaluation of the term (10) is immediate since it only depends on the number of non-null entries of the binary vector $\underline{\chi}$, on

the contrary, the prediction of the level of power within the S *RoIs*, to assess the fulfilment of the QoS requirements, would be computationally heavy whether using full-wave *EM* simulation tools based on *RT* techniques due to the large scale of the urban scenario at hand (Fig. 1).

In order to minimize the computational load, the *FFE* block is responsible for the off-line generation of a *DT* to estimate the coverage term (9) (i.e., $\tilde{\Phi}_{cov} \{\underline{\chi}\} \approx \Phi_{cov} \{\underline{\chi}\}$) so to efficiently predict the cost function value, $\Phi \{\underline{\chi}\}$, as follows (Fig. 3)

$$\tilde{\Phi} \{\underline{\chi}\} = \tilde{\Phi}_{cov} \{\underline{\chi}\} + \Phi_{cost} \{\underline{\chi}\}. \quad (12)$$

Towards this end, a Gaussian Process (*GP*) [39][42][43] is used to build the *DT* from the information embedded within an (off-line generated) training set of T input/output (*I/O*) pairs

$$\mathbb{T} = \{(\underline{\chi}^{(t)}; \Phi_{cov} \{\underline{\chi}^{(t)}\}); t = 1, \dots, T\} \quad (13)$$

randomly-chosen among the full set of $B = 2^K$ *EMSs* configurations ($T \ll B$). More specifically, the computationally-fast guess of (9) is given by

$$\tilde{\Phi}_{cov} \{\underline{\chi}\} = \nu + (\underline{\rho})' \underline{C}^{-1} (\underline{\Phi} - \underline{1}\nu) \quad (14)$$

where $\underline{\Phi} = \{\Phi_{cov} \{\underline{\chi}^{(t)}\}; t = 1, \dots, T\}'$ and $\nu = (\underline{1}' \underline{C}^{-1} \underline{1})^{-1} \underline{1}' \underline{C}^{-1} \underline{\Phi}$, $'$ being the transpose operator and $\underline{1}$ is a $(T \times 1)$ -size vector of unitary entries. Moreover, $\underline{C} = \{\Lambda(\underline{\chi}^{(p)}, \underline{\chi}^{(q)}); p, q = 1, \dots, T\}$ and $\underline{\rho} = \{\Lambda(\underline{\chi}, \underline{\chi}^{(t)}); t = 1, \dots, T\}$ are the training correlation matrix and the correlation vector of $\underline{\chi}$, respectively, the correlation between two input samples $\underline{\chi}^{(a/b)} \in \mathbb{R}^K$ being computed as

$$\Lambda(\underline{\chi}^{(a)}, \underline{\chi}^{(b)}) = \exp \left(- \sum_{k=1}^K \beta_k \left| \chi_k^{(a)} - \chi_k^{(b)} \right|^{\gamma_k} \right) \quad (15)$$

where $\underline{\beta} = \{\beta_k > 0; k = 1, \dots, K\}$ and $\underline{\gamma} = \{1 \leq \gamma_k \leq 2; k = 1, \dots, K\}$ are *GP* hyper-parameters determined during the off-line training phase by maximizing the likelihood function of \mathbb{T} [39][42][43].

3.4 SSE Block

By following the *SbD* guidelines [3] and according to the *no-free-lunch theorem* for optimization [44], the implementation of the *SSE* block is driven by the nature of the fitness function and of the solution space defined by the *PF* block (Sect. 3.2). As a matter of fact, it is profitable to select the most suitable optimization engine that assures a proper balance between exploration and local sampling of the solution space, while hill-climbing local minima of the cost function, to converge towards the global optimum of (8), $\underline{\chi}^{(opt)}$. Moreover, the optimization tool is required to properly handle (i.e., without considering time-expensive coding/decoding operations) the binary nature of the *DoFs* of the *OPP*.

Owing to these considerations, a binary genetic algorithm (*BGA*)-based strategy is adopted to find $\underline{\chi}^{(opt)}$ by evolving a population of P binary individuals, $\mathbb{P}_i = \{\underline{\chi}_i^{(p)}; p = 1, \dots, P\}$ ($i = 1, \dots, I$; i being the iteration index) during I iterations and according to the concepts of natural selection and genetic pressure [35][37]. Moreover, the *BGA* is here customized to take full advantage of the *SbD* framework for obtaining a considerable time saving by avoiding the time-costly assessment of each (i, p) -th ($i = 1, \dots, I$; $p = 1, \dots, P$) trial solution, $\underline{\chi}_i^{(p)}$, with a full-wave *EM* simulation. Towards this end, the iterative minimization of (8) leverages on the profitable interconnection of the *SSE* block with the *DT* derived in the *FFE* block (Sect. 3.3). Furthermore, the proposed implementation of the *BGA* benefits from the knowledge of the training set \mathbb{T} to enhance the convergence rate of the optimization process according to the “schemata theorem” of *GAs* [38], which states that “above average schemata receive exponentially increasing trials in subsequent generations”. Accordingly, since the probability to yield “good” schemata [38] by randomly-selecting P binary chromosomes from the whole set of B ($B \triangleq 2^K$) admissible binary sequences ($P \ll B$) is generally low, the individuals of the initial population \mathbb{P}_0 are chosen among the fittest ones of the T solutions of the training set, $\{\underline{\chi}^{(t)}; t = 1, \dots, T\}$.

The sequence of procedural steps carried out in the *SEE* block is summarized in the following.

1. *Initialization* ($i = 0$) - Sort the training solutions of \mathbb{T} , $\{\underline{\chi}^{(t)}; t = 1, \dots, T\}$, according to their fitness values, $\varphi\{\underline{\chi}^{(t)}\}$ ($t = 1, \dots, T$), and build the sorted set \mathbb{R}_0 ($\mathbb{R}_0 = \{\underline{\chi}_0^{(r)}; r = 1, \dots, T\}$ being $\underline{\chi}_0^{(1)} = \arg(\min_{t=1, \dots, T}[\Phi\{\underline{\chi}^{(t)}\}])$ and $\underline{\chi}_0^{(T)} = \arg(\max_{t=1, \dots, T}$

$[\Phi \{\underline{\chi}^{(t)}\}]$). Create the initial population \mathbb{P}_0 ($\mathbb{P}_0 = \{\underline{\chi}_0^{(p)}; p = 1, \dots, P\}$) by randomly selecting P individuals out of the $\frac{T}{2}$ elements of \mathbb{R}_0 with fitness values above the median;

2. Optimization Loop ($i = 1, \dots, I$)

- (a) Generate a new population of offsprings, \mathbb{P}_i , by applying the genetic operators to the population of the parents, $\mathbb{P}_{(i-1)}$, as follows

$$\mathbb{P}_i = \mathcal{M} \left\{ \mathcal{C} \left\{ \mathcal{S} \left\{ \mathbb{P}_{(i-1)} \right\} \right\} \right\} \quad (16)$$

where the “mating pool” $\mathbb{P}_{(i-1)}^S$ ($\mathbb{P}_{(i-1)}^S \triangleq \mathcal{S} \left\{ \mathbb{P}_{(i-1)} \right\}$) is derived by undergoing $\mathbb{P}_{(i-1)}$ to the roulette wheel selection, \mathcal{S} [35], while the single-point cross-over, \mathcal{C} , is applied with probability δ^C to generate the intermediate set of individuals, $\mathbb{P}_{(i-1)}^C$ ($\mathbb{P}_{(i-1)}^C \triangleq \mathcal{C} \left\{ \mathbb{P}_{(i-1)}^S \right\}$), which is successively processed by the mutation operator, \mathcal{M} , with mutation and bit-mutation probabilities equal to δ_1^M and δ_2^M , respectively [35];

- (b) Exploit the *FFE* block (Sect. 3.3) to predict, according to (14) and (12), the fitness function of each individual of \mathbb{P}_i , $\{\varphi \left\{ \underline{\chi}_i^{(p)} \right\}; p = 1, \dots, P\}$. Select through elitism [35] the fittest individual generated until the current i -th iteration, $\underline{\chi}^{(i)} = \arg \left[\min_{p=1, \dots, P} \min_{j=1, \dots, i} \tilde{\Phi} \left\{ \underline{\chi}_j^{(p)} \right\} \right]$;
- (c) Check the convergence condition (i.e., $i = I$ or $\Phi \left\{ \underline{\chi}^{(i)} \right\} \leq \xi$, ξ being a user-defined threshold). If the convergence has been reached, then goto to the “*Output Phase*” (3.), otherwise update the iteration index ($i \rightarrow i + 1$) and repeat the “*Optimization Loop*” (2.);

3. Output Phase - Output the *OPP* solution given by

$$\underline{\chi}^{(opt)} = \arg \left[\min_{p=1, \dots, P} \tilde{\Phi} \left\{ \underline{\chi}_i^{(p)} \right\} \right]. \quad (17)$$

4 Numerical Validation

The goal of this section is to assess the capabilities and the potentialities of the approach to enhance the wireless coverage and the overall *QoS* in large urban scenarios thanks to the optimal deployment of *EMS*s on the building facades.

Such an assessment has been carried out in a real-world scenario by considering the Gardolo district of the city of Trento (Italy) as the benchmark test-bed (Fig. 5). As it can be inferred from the satellite image [Fig. 5(a)] taken from the Google Maps website [46], the selected area Ξ is a square region 1 [Km]-sided that comprises several streets, a railway, and a quite dense distribution of civil, commercial, and industrial buildings.

The actual position of the *BTS*, which serves the users in Ξ , is $\mathbf{r}_\Psi = (3.95 \times 10^2, 5.79 \times 10^2, 30)$ [m] and it has been extracted from the official *BTS* cartography publicly accessible on the website of the city of Trento [45] [Fig. 5(b)]. The site consists of $V = 3$ sectors having an angular extension equal to $\Delta\phi_\Psi = 120$ [deg] in azimuth, pointed towards the directions $\phi_\Psi^{(v)} = (v - 1) \times 120$ [deg] ($v = 1, \dots, V$), with a mechanical down-tilt of $\Delta\theta_\Psi = 2$ [deg] in elevation [51][52][53]. Each v -th ($v = 1, \dots, V$) sector has been assumed to be illuminated by a panel of the *BTS*, which is composed by a planar array (Fig. 6) of $N = (13 \times 2)$ $\frac{\lambda}{2}$ -spaced slot-coupled dual-polarized (slant-45) square patch radiators working at $f = 3.5$ [GHz] with a ground plane of size $(L_y \times L_z) = (1.75 \times 7)$ [λ] [52][53] (see the inset in Fig. 6). Such an antenna array has been accurately modeled in the Ansys *HFSS* simulation suite [47] to take into account all mutual coupling effects. The co-polar gain pattern for the +45-polarization operation, $G_{+45}(\theta, \phi)$ [48], is shown in Fig. 6, the maximum gain being $G_{+45}^{\max} = \max_{(\theta, \phi)} G_{+45}(\theta, \phi) = 16.3$ [dBi] ⁽²⁾.

As for the wireless coverage, the power distribution in Ξ (Fig. 5) has been computed with the *RT*-based Altair WinProp simulator [49]. Towards this end, the exact position, orientation, and dimensions of each building has been first extracted from the OpenStreetMap (*OSM*) Geographic Information System (*GIS*) database [50] [Fig. 5(b)], then it has been imported into WinProp to generate the *EM* simulation scenario in Fig. 5(c) where the buildings have been

⁽²⁾For symmetry reasons, the co-polar pattern for the -45 operation, $G_{-45}(\theta, \phi)$, coincides with $G_{+45}(\theta, \phi)$. Accordingly, all the results reported in the following refers to the +45 operation of the *BTS*.

assumed to be made of concrete with relative permittivity $\varepsilon_r = 4$ and conductivity $\sigma = 10^{-2}$ [S/m] [54][56]. Figure 7(a) shows the power distribution (i.e., $\mathcal{P}_0(\mathbf{r})$, $\mathbf{r} \in \Xi$) computed at a standard user height of $h = 1.5$ [m] [55] on a grid of points uniformly-spaced ($\Delta_x = \Delta_y = 5$ [m] being the spacing along x - and y -axes), when feeding the *BTS* panels with an input power of $\mathcal{P}_{in}^{(v)} = 20$ [W], $v = 1, \dots, V$ [52][53]. In addition to the standard attenuation due to the path loss, the distribution of the power radiated by the *BTS* turns out to be strongly affected by the presence of the buildings, which cause shadowing effects as well as wave-guiding phenomena (e.g., canyoning along the main streets).

The *RoIs* in Ξ have been identified by thresholding ($\mathcal{P}_{th} = -65$ [dBm]⁽³⁾ being the value of the coverage threshold) the distribution of \mathcal{P}_0 . The binary map in Fig. 7(b) shows $S = 2$ *RoIs*. The first one has an area of $A(\Omega^{(1)}) = 1225$ [m^2] ($M^{(1)} = 49$) and it is centered at $\mathbf{r}_{\Omega}^{(1)} = (411, 698, 1.5)$ [m] [Fig. 7(b) and Figs. 8(a)], while the other is located at $\mathbf{r}_{\Omega}^{(2)} = (123, 280, 1.5)$ [m] and extends on a support of $A(\Omega^{(2)}) = 1075$ [m^2] ($M^{(2)} = 43$) [Fig. 7(b) and Figs. 8(b)].

According to the proposed planning method (Sect. 2), a set of $W^{(s)}$ ($W^{(1)} = 8$ [Fig. 8(c)]; $W^{(2)} = 12$ [Fig. 8(d)]) building facades has been chosen into each neighboring square region, $\Pi^{(s)}$, of a *RoI* $\Omega^{(s)}$ ($s = 1, \dots, S$). Then, the complete set of $K = 20$ *EMSs* has been off-line synthesized in the *EMSD* block (Fig. 3 - Sect. 3.1) by assuming an installation quota of $z_w^{(s)} = (H_w^{(s)} - 2)$ [m] from the ground level (Fig. 4), $H_w^{(s)}$ being the height of the (w, s) -th ($w = 1, \dots, W^{(s)}$, $s = 1, \dots, S$) wall, $\tau_w^{(s)}$, in the *OSM* database [50]. More specifically, each *EMS* has been implemented [4] with a properly-tailored pattern of $L = (50 \times 50)$ square-shaped unit cells (i.e., $O = 1$) printed on a support of $A(\Gamma_w^{(s)}) = (2.14 \times 2.14)$ [m^2] ($w = 1, \dots, W^{(s)}$, $s = 1, \dots, S$) over a Rogers RT/duroid 5870 substrate ($\varepsilon_r = 2.33$, $\tan \delta = 1.2 \times 10^{-3}$) of thickness 3.7×10^{-2} [λ].

The *OPP* at hand is then solved by sampling the B -size ($B \approx 1.05 \times 10^6$ - Tab. I) solution space of the admissible *EMSs* deployments with the *SbD*-based approach (Sect. 3). Towards this end, the *SbD* control parameters have been set according to the state-of-the-art guidelines [3][35]: $T = 4 \times 10^3$, $P = 40$, $I = 10^3$, $\delta^C = 8 \times 10^{-1}$, $\delta_1^M = 10^{-1}$, and $\delta_2^M = 10^{-2}$.

⁽³⁾The value $\mathcal{P}_{th} = -65$ [dBm] is often assumed as the reference signal received power (*RSRP*) to support advanced high-throughput wireless services (e.g., high-definition video streaming [57]).

The final ($i = I$) outcome of the planning process is summarized in Fig. 9 where the thresholded maps of the distribution of power received in $\Omega^{(1)}$ [Fig. 9(a)] and $\Omega^{(2)}$ [Fig. 9(b)] are reported along with the positions of the selected *EMSs*. There are $Q^{(opt)} = 7$ *EMSs* (i.e., $\underline{\Gamma}^{(opt)} = \{\Gamma_1^{(1)}, \Gamma_2^{(1)}, \Gamma_7^{(1)}, \Gamma_2^{(2)}, \Gamma_4^{(2)}, \Gamma_5^{(2)}, \Gamma_6^{(2)}\}$ - Tab. I), $Q^{(opt)}|_{s=1} = 3$ [i.e., $\underline{\Gamma}^{(opt)}|_{s=1} = \{\Gamma_1^{(1)}, \Gamma_2^{(1)}, \Gamma_7^{(1)}\}$ - Fig. 9(a)] and $Q^{(opt)}|_{s=2} = 4$ [$\underline{\Gamma}^{(opt)}|_{s=2} = \{\Gamma_2^{(2)}, \Gamma_4^{(2)}, \Gamma_5^{(2)}, \Gamma_6^{(2)}\}$ - Fig. 9(b)] for $\Omega^{(1)}$ and $\Omega^{(2)}$, respectively. Thanks to the reduction of the coverage term (9) of about two orders of magnitude with respect to the “nominal” scenario without *EMSs* (i.e., $\frac{\Phi_{cov}\{\underline{\chi}=0\}}{\Phi_{cov}\{\underline{\chi}^{(opt)}\}} = 1.19 \times 10^{-2}$ - Tab. I), there is a remarkable enhancement of the level of the power received in the *RoIs*. Indeed, the coverage condition always holds true in $\Omega^{(1)}$ [i.e., $\mathcal{P}(\mathbf{r}|\underline{\chi}^{(opt)}) > \mathcal{P}_{th}$, $\mathbf{r} \in \Omega^{(1)}$ - Fig. 9(a) vs. Fig. 8(a)], while only few locations of $\Omega^{(2)}$ are under the power threshold \mathcal{P}_{th} , $\Delta A(\Omega^{(2)}) = 86\%$ [$\Delta A(\Omega^{(s)}) \triangleq \frac{A(\Omega^{(s)}|\underline{\chi}=0) - A(\Omega^{(s)}|\underline{\chi}^{(opt)})}{A(\Omega^{(s)}|\underline{\chi}=0)}$; ($s = 1, \dots, S$)] being the widening of the coverage surface [Fig. 9(b) vs. Fig. 8(b)] ⁽⁴⁾.

To point out the coverage improvement enabled by the *EMSs*, the thresholded maps of the power gap $\Delta\mathcal{P}(\mathbf{r})$ [$\Delta\mathcal{P}(\mathbf{r}) \triangleq \mathcal{P}(\mathbf{r}|\underline{\chi}^{(opt)}) - \mathcal{P}_0(\mathbf{r})$] are shown, as well [Figs. 9(c)-9(d)]. One can observe that the received power has been increased (i.e., $\Delta\mathcal{P}(\mathbf{r}) > 0$) over a wide region around both the *RoIs* centers, while the red pixels always correspond to limited/negligible reductions of power level (i.e., $\Delta\mathcal{P}(\mathbf{r}) \geq -1.5$ [dBm]).

Let us now focus on $\Omega^{(1)}$ to investigate on the “effect/impact” of each q -th ($q = 1, \dots, Q^{(opt)}|_{s=1} = 3$) *EMS* on the wireless coverage. Towards this purpose, Figure 10 gives the behavior of the cumulative density function (CDF) of the received power, Θ , which is defined as

$$\Theta\{\mathcal{P}(\mathbf{r})|\hat{\mathcal{P}}\} = \Pr\{\mathcal{P}(\mathbf{r}) \leq \hat{\mathcal{P}}\} \quad (18)$$

where $\Pr\{\cdot\}$ denotes the probability function and $\hat{\mathcal{P}} \in [-70, -50]$ [dBm], computed over a circular region of radius $\zeta = 40$ [m] and centered in $\mathbf{r}_\Omega^{(1)}$ [Fig. 9(a)]. It turns out that there is a progressive improvement of the wireless coverage (i.e., $\Theta\{\mathcal{P}(\mathbf{r})|\mathcal{P}_{th}\}|_{Q^{(1)}-1} > \Theta\{\mathcal{P}(\mathbf{r})|\mathcal{P}_{th}\}|_{Q^{(1)}} > \Theta\{\mathcal{P}(\mathbf{r})|\mathcal{P}_{th}\}|_{Q^{(1)}+1}$) starting from the “nominal” case [i.e., $\Theta\{\mathcal{P}_0(\mathbf{r})|\mathcal{P}_{th}\} = 30.2\%$ - Fig. 8(a)] up to the *EMSs* planning at convergence [i.e., $\Theta\{\mathcal{P}(\mathbf{r}|\underline{\chi}^{(opt)})|\mathcal{P}_{th}\} = 0$

⁽⁴⁾It is worth pointing out that the coverage improvement in $\Omega^{(2)}$ is intrinsically a harder task than that for $\Omega^{(1)}$ because of the larger distance, R , of the *BTS* from $\Omega^{(2)}$ (i.e., $R(\mathbf{r}_\Psi, \mathbf{r}_\Omega^{(1)}) \approx 123$ [m] vs. $R(\mathbf{r}_\Psi, \mathbf{r}_\Omega^{(2)}) \approx 405$ [m] - Fig. 7).

% - Fig. 9(a)]. For completeness, Figure 11 shows the thresholded maps for the two intermediate sub-optimal configurations comprising $Q^{(1)} = 1$ [$\Theta \{ \mathcal{P}(\mathbf{r}) | \mathcal{P}_{th} \} |_{Q^{(1)}=1} = 14.2$ % - Fig. 11(a) and Fig. 10] and $Q^{(1)} = 2$ EMSs [$\Theta \{ \mathcal{P}(\mathbf{r}) | \mathcal{P}_{th} \} |_{Q^{(1)}=2} = 2.5$ % - Fig. 11(b) and Fig. 10].

Similar results have been yielded for the *RoI* $\Omega^{(2)}$ (Fig. 12), as well. More in detail, the *SbD*-derived EMSs distribution reduces the probability of being below the coverage threshold of $\mathcal{P}_{th} = -65$ [dBm] from $\Theta \{ \mathcal{P}(\mathbf{r}) | \mathcal{P}_{th} \} |_{Q^{(2)}=0} = 26.0$ % [Fig. 8(b)] down to $\Theta \{ \mathcal{P}(\mathbf{r}) | \mathcal{P}_{th} \} |_{Q^{(2)}=4} = 4.7$ % [Fig. 9(b)], being $\Theta \{ \mathcal{P}(\mathbf{r}) | \mathcal{P}_{th} \} |_{Q^{(2)}=1} = 25.2$ % [Fig. 13(a)], $\Theta \{ \mathcal{P}(\mathbf{r}) | \mathcal{P}_{th} \} |_{Q^{(2)}=2} = 17.2$ % [Fig. 13(b)], and $\Theta \{ \mathcal{P}(\mathbf{r}) | \mathcal{P}_{th} \} |_{Q^{(2)}=3} = 9.3$ % [Fig. 13(c)].

As for the computational issues, the *SbD* method assures a time saving of about $\Delta t_{sav} \approx 90\%$ ⁽⁵⁾ ($\Delta t_{sav} \triangleq \frac{(P \times I) - T}{(P \times I)}$) [3] with respect to a standard optimization, mainly thanks to the exploitation of the *DT* for the coverage assessment (Sect. 3.3) during the iterative process.

The second test case of the numerical validation is concerned with a more challenging *OPP*, the power threshold being set to $\mathcal{P}_{th} = -60$ [dBm]. Owing to the harder requirement, two additional *RoIs* appear on the same scenario Ξ of the previous example ($S = 4$ - Fig. 14), namely the *RoI* $\Omega^{(3)}$ ($\mathbf{r}_{\Omega}^{(3)} = (313, 914, 1.5)$ [m], $M^{(3)} = 74$, and $A(\Omega^{(3)}) = 1850$ [m^2]) and the *RoI* $\Omega^{(4)}$ ($\mathbf{r}_{\Omega}^{(4)} = (363, 396, 1.5)$ [m], $M^{(4)} = 59$, and $A(\Omega^{(4)}) = 1475$ [m^2]). Therefore, $W^{(3)} = 10$ [Fig. 15(a)] and $W^{(4)} = 8$ [Fig. 15(b)] new EMSs have been designed in the *EMSD* block (Sect. 3.1) for a potential deployment on the “candidate” building facades in $\Pi^{(3)}$ [Fig. 15(a)] and $\Pi^{(4)}$ [Fig. 15(b)]. Due to the higher cardinality of the solution space (i.e., $K = 38 \rightarrow B = 2.75 \times 10^{11}$ - Tab. I), a bigger training set \mathbb{T} of $T = 7.6 \times 10^3$ *I/O* pairs has been generated to build the *DT* (Sect. 3.3), while the population size of the *BGA* has been increased to $P = 76$ [3][35].

At the convergence, the coverage maps in Fig. 16 have been synthesized by installing $Q^{(opt)} = 24$ EMSs ($\Phi_{cost} \{ \underline{\chi}^{(opt)} \} = 6.32 \times 10^{-1}$ - Tab. I). As expected, the number of EMSs deployed for $\Omega^{(1)}$ [i.e., $Q^{(opt)}|_{s=1} = 6$ - Figs. 16(a)-16(c)] and for $\Omega^{(2)}$ [i.e., $Q^{(opt)}|_{s=2} = 10$ - Figs. 16(d)-16(f)] is larger with respect to the previous benchmark because of the more demanding

⁽⁵⁾Considering that the average simulation time for evaluating the received power distribution associated to one trial guess of the *SbD-DoFs* vector $\underline{\chi}$ is equal to $\Delta t_{sim} = 75$ [sec] on a standard laptop equipped with an Intel(R) Core(TM) i5-8250U CPU @ 1.60GHz and 16 [GB] of RAM memory, it turns out that the time for a serial assessment of all B configurations would be equal to $\Delta t_{sim}^{enum} = (B \times \Delta t_{sim}^{avg}) \approx 910$ [days].

requirement on \mathcal{P}_{th} . Moreover, there has been an improvement of the QoS within the $S = 4$ $RoIs$ (see the left column vs. the middle column in Fig. 16) as quantitatively assessed by the reduction of the value of coverage term (9) with respect to the scenario without $EMSs$ (i.e., $\frac{\Phi_{cov}\{\chi=0\}}{\Phi_{cov}\{\chi^{(opt)}\}} = 2.59 \times 10^{-1}$ - Tab. I). The effectiveness of the proposed planning method can be also clearly inferred from the analysis of the $\Delta\mathcal{P}(\mathbf{r})$ maps (right column of Fig. 16) where the power level increases within large areas centered on the $RoIs$ centers, $\{\mathbf{r}_{\Omega}^{(s)}; s = 1, \dots, S\}$.

The positive outcome on the $EMSs$ planning is also confirmed, from a statistical viewpoint, by the $CDFs$ in Fig. 17. For instance, let us analyze the case of the $RoI \Omega^{(4)}$. It turns out that the deployment of $Q^{(4)} = Q^{(opt)}|_{s=4} = 3$ $EMSs$ reduces the probability of being below the QoS threshold of $\mathcal{P}_{th} = -60$ [dBm] from $\Theta\{\mathcal{P}(\mathbf{r})|\mathcal{P}_{th}\}|_{Q^{(4)}=0} = 49.2\%$ [Fig. 16(l)] down to $\Theta\{\mathcal{P}(\mathbf{r})|\mathcal{P}_{th}\}|_{Q^{(4)}=3} = 8.3\%$ [Fig. 16(n)] with a reduction of the “blind” area of about $\Delta A\{\Omega^{(4)}\} \approx 86.4\%$.

5 Conclusions

In the framework of the emerging *SEME* paradigm, the planning of passive/low-cost $EMSs$ to enhance the QoS in large-scale urban propagation scenarios has been addressed. An innovative *SbD*-based strategy has been proposed to solve the arising *OPP* by determining optimal trade-off solutions, which jointly maximize the level of power received within “no-coverage/low- QoS ” $RoIs$ and minimize the overall cost and environmental impact.

The numerical assessment, on a real-world test-bed, has proved the feasibility of the proposed strategy for the *SEME* implementation as well as the effectiveness of the proposed planning method. By considering both different $RoIs$ and distances from the *BTS* as well as various values of the coverage threshold \mathcal{P}_{th} , effective $EMSs$ deployments have been obtained with a significant computational efficiency, as well.

Future works, beyond the scope of this paper, will be aimed at extending the proposed approach to deal with the planning of mixed scenarios involving both *RISs* and *IAB* nodes.

Acknowledgements

This work benefited from the networking activities carried out within the Project “CYBER-PHYSICAL ELECTROMAGNETIC VISION: Context-Aware Electromagnetic Sensing and Smart Reaction (EMvisioning)” (Grant no. 2017HZJXSZ)“ funded by the Italian Ministry of Education, University, and Research under the PRIN2017 Program (CUP: E64I19002530001). Moreover, it benefited from the networking activities carried out within the Project “SPEED” (Grant No. 61721001) funded by National Science Foundation of China under the Chang-Jiang Visiting Professorship Program, the Project ‘Inversion Design Method of Structural Factors of Conformal Load-bearing Antenna Structure based on Desired EM Performance Interval’ (Grant no. 2017HZJXSZ) funded by the National Natural Science Foundation of China, and the Project ‘Research on Uncertainty Factors and Propagation Mechanism of Conformal Load-bearing Antenna Structure’ (Grant No. 2021JZD-003) funded by the Department of Science and Technology of Shaanxi Province within the Program Natural Science Basic Research Plan in Shaanxi Province. A. Massa wishes to thank E. Vico for her never-ending inspiration, support, guidance, and help.

References

- [1] M. Di Renzo, M. Debbah, D.-T. Phan-Huy, A. Zappone, M.-S. Alouini, C. Yuen, V. Sciancalepore, G.C. Alexandropoulos, J. Hoydis, H. Gacanin, J. de Rosny, A. Bounceur, G. Lerosey, and M. Fink, “Smart radio environments empowered by reconfigurable AI metasurfaces: An idea whose time has come,” *EURASIP J. Wireless Commun. Netw.*, vol. 2019, no. 129, pp. 1-20, 2019.
- [2] M. Di Renzo, A. Zappone, M. Debbah, M.-S. Alouini, C. Yuen, J. de Rosny, and S. Tretyakov, “Smart radio environments empowered by reconfigurable intelligent surfaces: How it works, state of research, and the road ahead,” *IEEE J. Sel. Areas Commun.*, vol. 38, no. 11, pp. 2450-2525, Nov. 2020.

- [3] A. Massa, A. Benoni, P. Da R  , S. K. Goudos, B. Li, G. Oliveri, A. Polo, P. Rocca, and M. Salucci, "Designing smart electromagnetic environments for next-generation wireless communications," *Telecom*, Invited Feature Paper, vol. 2, no. 2, pp. 213-221, 2021.
- [4] G. Oliveri, P. Rocca, M. Salucci, and A. Massa, "Holographic smart EM skins for advanced beam power shaping in next generation wireless environments," *IEEE J. Multiscale Multiphys. Comput. Tech.*, to be published. [Online]. Available: arXiv:2106.10932.
- [5] C. Huang, S. Hu, G. C. Alexandropoulos, A. Zappone, C. Yuen, R. Zhang, M. Di Renzo, and M. Debbah, "Holographic MIMO surfaces for 6G wireless networks: Opportunities, challenges, and trends," *IEEE Wireless Commun.*, vol. 27, no. 5, pp. 118-125, Oct. 2020.
- [6] R. L. Haupt, *Wireless Communications Systems: An Introduction*. Hoboken, NJ, USA: John Wiley & Sons, IEEE Press, 2020.
- [7] C. Cox, *An Introduction to 5G: The New Radio, 5G Network and Beyond*. Hoboken, NJ, USA: John Wiley & Sons, 2021.
- [8] M. Bennis, M. Debbah, and H. V. Poor, "Ultrareliable and low-latency wireless communication: tail, risk, and scale," *Proc. IEEE*, vol. 106, no. 10, pp. 1834-1853, Oct. 2018.
- [9] W. Hong, Z. H. Jiang, C. Yu, D. Hou, H. Wang, C. Guo, Y. Hu, L. Kuai, Y. Yu, Z. Jiang, Z. Chen, J. Chen, Z. Yu, J. Zhai, N. Zhang, L. Tian, F. Wu, G. Yang, Z.-C. Hao, and J. Y. Zhou, "The role of millimeter-wave technologies in 5G/6G wireless communications," *IEEE J. Microw.*, vol. 1, no. 1, pp. 101-122, Jan. 2021.
- [10] G. Oliveri, G. Gottardi and A. Massa, "A new meta-paradigm for the synthesis of antenna arrays for future wireless communications," *IEEE Trans. Antennas Propag.*, vol. 67, no. 6, pp. 3774-3788, Jun. 2019.
- [11] E. Basar, M. Di Renzo, J. De Rosny, M. Debbah, M.-S. Alouini, and R. Zhang, "Wireless communications through reconfigurable intelligent surfaces," *IEEE Access*, vol. 7, pp. 116753-116773, 2019.

- [12] A. Diaz-Rubio, S. Kosulnikov, and S. Tretyakov, "On the integration of reconfigurable intelligent surfaces in real-world environments," TechRxiv, 2021 [Online]. Available: <https://doi.org/10.36227/techrxiv.16628260.v1>
- [13] G. C. Trichopoulos, P. Theofanopoulos, B. Kashyap, A. Shekhawat, A. Modi, T. Osman, S. Kumar, A. Sengar, A. Chang, and A. Alkhateeb, "Design and evaluation of reconfigurable intelligent surfaces in real-world environment," 2021. [Online]. Available: arXiv:2109.07763.
- [14] F. H. Danufane, M. D. Renzo, J. de Rosny, and S. Tretyakov, "On the path-loss of reconfigurable intelligent surfaces: An approach based on Green's theorem applied to vector fields," *IEEE Trans. Commun.*, vol. 69, no. 8, pp. 5573-5592, Aug. 2021.
- [15] Q. Wu, S. Zhang, B. Zheng, C. You, and R. Zhang, "Intelligent reflecting surface-aided wireless communications: A tutorial," *IEEE Trans. Commun.*, vol. 69, no. 5, pp. 3313-3351, May 2021.
- [16] C. Pan, H. Ren, K. Wang, J. F. Kolb, M. El Kashlan, M. Chen, M. Di Renzo, Y. Hao, J. Wang, A. L. Swindlehurst, X. You, and L. Hanzo, "Reconfigurable intelligent surfaces for 6G systems: principles, applications, and research directions," *IEEE Commun. Mag.*, vol. 59, no. 6, pp. 14-20, Jun. 2021.
- [17] E. Bjornson, O. Ozdogan, and E. G. Larsson, "Reconfigurable intelligent surfaces: three myths and two critical questions," *IEEE Commun. Mag.*, vol. 58, no. 12, pp. 90-96, Dec. 2020.
- [18] X. Yuan, Y. -J. A. Zhang, Y. Shi, W. Yan, and H. Liu, "Reconfigurable-intelligent-surface empowered wireless communications: Challenges and opportunities," *IEEE Wireless Commun.*, vol. 28, no. 2, pp. 136-143, Apr. 2021.
- [19] C. Nguyen, O. Georgiou, G. Gradoni, and M. Di Renzo, "Wireless fingerprinting localization in smart environments using reconfigurable intelligent surfaces," *IEEE Access*, vol. 9, pp. 135526-135541, 2021.

- [20] G. Gradoni and M. Di Renzo, "End-to-end mutual coupling aware communication model for reconfigurable intelligent surfaces: An electromagnetic-compliant approach based on mutual impedances," *IEEE Wireless Commun. Lett.*, vol. 10, no. 5, pp. 938-942, 2021.
- [21] K. Liu, Z. Zhang, L. Dai, S. Xu, and F. Yang, "Active reconfigurable intelligent surface: fully-connected or sub-connected?," *IEEE Commun. Lett.*, pp. 1-1, 2021.
- [22] C. Huang, A. Zappone, G. C. Alexandropoulos, M. Debbah, and C. Yuen, "Reconfigurable intelligent surfaces for energy efficiency in wireless communication," *IEEE Trans. Wireless Commun.*, vol. 18, no. 8, pp. 4157-4170, 2019.
- [23] A. Pitilakis, O. Tsilipakos, F. Liu, K. M. Kossifos, A. C. Tasolamprou, D.-H. Kwon, M. S. Mirmoosa, D. Manassis, N. V. Kantartzis, C. Liaskos, M. A. Antoniadis, J. Georgiou, C. M. Soukoulis, M. Kafesaki, and S. A. Tretyakov, "A multi-functional reconfigurable metasurface: electromagnetic design accounting for fabrication aspects," *IEEE Trans. Antennas Propag.*, vol. 69, no. 3, pp. 1440-1454, Mar. 2021.
- [24] Z. Wang, X. Pan, F. Yang, S. Xu, M. Li, and D. Su, "Design, analysis, and experiment on high-performance orbital angular momentum beam based on 1-bit programmable metasurface," *IEEE Access*, vol. 9, pp. 18585-18596, 2021.
- [25] A. Casolaro, A. Toscano, A. Alú, and F. Bilotti, "Dynamic beam steering with reconfigurable metagratings," *IEEE Trans. Antennas Propag.*, vol. 68, no. 3, pp. 1542-1552, Mar. 2020.
- [26] F. Yang and Y. Rahmat-Samii, *Surface Electromagnetics with Applications in Antenna, Microwave, and Optical Engineering*. Cambridge, UK: Cambridge University Press, 2019.
- [27] H. Yang, X. Cao, F. Yang, J. Gao, S. Xu, M. Li, X. Chen, Y. Zhao, Y. Zheng, and S. Li, "A programmable metasurface with dynamic polarization, scattering and focusing control," *Sci. Rep.*, no. 6, pp. 35692, 2016.
- [28] J. C. Soric, R. Fleury, A. Monti, A. Toscano, F. Bilotti, and A. Alú, "Controlling scattering and absorption with metamaterial covers," *IEEE Trans. Antennas Propag.*, vol. 62, no. 8, pp. 4220-4229, Aug. 2014.

- [29] X. Fang, M. Li, D. Ding, F. Bilotti, and R. Chen, "Design of in-phase and quadrature two paths space-time-modulated metasurfaces," TechRxiv, 2021 [Online]. Available: 10.36227/techrxiv.15086538.v1.
- [30] H. Yang, F. Yang, S. Xu, M. Li, X. Cao, and J. Gao, "A 1-bit multipolarization reflectarray element for reconfigurable large-aperture antennas," *IEEE Antennas Wireless Propag. Lett.*, vol. 16, pp. 581-584, 2017.
- [31] P. Nayeri, F. Yang, and A. Z. Elsherbeni, "Beam-scanning reflectarray antennas: A technical overview and state of the art," *IEEE Antennas Propag. Mag.*, vol. 57, no. 4, pp. 32-47, Apr. 2015.
- [32] J. Tang, S. Xu, F. Yang, and M. Li, "Design and measurement of a reconfigurable transmitarray antenna with compact varactor-based phase shifters," *IEEE Antennas Wireless Propag. Lett.*, vol. 20, no. 10, pp. 1998-2002, 2021.
- [33] A. Massa and M. Salucci, "On the design of complex *EM* devices and systems through the System-by-Design paradigm - A framework for dealing with the computational complexity," *IEEE Trans. Antennas Propag.*, DOI: 10.1109/TAP.2021.3111417.
- [34] M. Salucci, G. Oliveri, M. A. Hannan, and A. Massa, "System-by-Design paradigm-based synthesis of complex systems: The case of spline-contoured 3D radomes," *IEEE Antennas Propag. Mag.*, (DOI: 10.1109/MAP.2021.3099719).
- [35] P. Rocca, M. Benedetti, M. Donelli, D. Franceschini, and A. Massa, "Evolutionary optimization as applied to inverse scattering problems," *Inv. Prob.*, Invited Paper, vol. 24, pp. 1-41, 2009.
- [36] P. Rocca, G. Oliveri, and A. Massa, "Differential evolution as applied to electromagnetics," *IEEE Antennas Propag. Mag.*, vol. 53, no. 1, pp. 38-49, Feb. 2011.
- [37] S. K. Goudos, *Emerging Evolutionary Algorithms for Antennas and Wireless Communications*. IET, 2021 (ISBN 1785615521).

- [38] D. E. Goldberg, *Genetic Algorithms in Search, Optimization, and Machine Learning*. Boston, MA: Addison-Wesley, 1989.
- [39] A. Massa, G. Oliveri, M. Salucci, N. Anselmi, and P. Rocca, "Learning-by-examples techniques as applied to electromagnetics," *J. Electromagn. Waves Appl.*, vol. 32, no. 4, pp. 516-541, 2018.
- [40] S. Y. Liao, "Measurements and computations of electric field intensity and power density," *IEEE Trans. Instrum. Meas.*, vol. IM-26, no. 1, pp. 53-57, Mar. 1977.
- [41] C. Balanis, *Antenna theory: analysis and design*. Hoboken, N.J.: Wiley, 2016.
- [42] A. I. J. Forrester, A. Sobester, and A. J. Keane, *Engineering Design via Surrogate Modelling: A Practical Guide*. Hoboken, N.J.: John Wiley & Sons, 2008.
- [43] D. R. Jones, M. Schonlau, and W.J. Welch, "Efficient global optimization of expensive black-box functions," *J. Global Opt.*, vol. 13, pp. 455-492, 1998.
- [44] D. H. Wolper and W. G. Mcready, "No free lunch theorem for optimization," *IEEE Trans. Evol. Comput.*, vol. 1, no. 1, pp. 67-82, Apr. 1997.
- [45] Comune di Trento, *Official Radio Basestation Carthography Web App*. Accessed on: October 02, 2021. [Online]. Available: <http://webapps.comune.trento.it/mapaccel/?project=ambiente&view=elettromagnetismo&locale=it>
- [46] Google, Google Maps. Accessed on: October 02, 2021. [Online]. Available: <https://www.google.com/maps>
- [47] ANSYS Electromagnetics Suite - HFSS (2021). ANSYS, Inc.
- [48] X. Quan, R. Li, Y. Fan, and D. E. Anagnostou, "Analysis and design of a 45° Slant-Polarized omnidirectional antenna," *IEEE Trans. Antennas Propag.*, vol. 62, no. 1, pp. 86-93, Jan. 2014
- [49] Altair Winprop 2020, Altair Engineering, Inc., www.altairhyperworks.com/feko

- [50] OpenStreetMap. Accessed on: October 02, 2021. [Online]. Available: <https://www.openstreetmap.org/>
- [51] J. Yang, M. Ding, G. Mao, Z. Lin, D. Zhang, and T. H. Luan, "Optimal base station antenna downtilt in downlink cellular networks," *IEEE Trans. Wireless Commun.*, vol. 18, no. 3, pp. 1779-1791, Mar. 2019.
- [52] 3G Americas, "MIMO and smart antennas for 3G and 4G wireless system - practical aspects and deployment considerations", May 2010.
- [53] 4G Americas, "MIMO and smart antennas for mobile broadband systems", Jun. 2013.
- [54] -, *Effects of building materials and structures on radio wave propagation above about 100 MHz*, Rec. ITU-R P.2040-1, International Telecommunication Union, Geneva, Switzerland, Jul. 2015.
- [55] 3GPP, "Technical Specification Group Radio Access Network - Study on 3D channel model for LTE," Technical Report, TR 36.873, v. 12.2.0, 2015-06.
- [56] D. J. Daniels, Ed., *Ground Penetrating Radar* (2nd Ed.), London, UK: The Institution of Electrical Engineers, 2004.
- [57] GSMA, "4G/5G network experience evaluation guideline", Feb. 2020.

FIGURE CAPTIONS

- **Figure 1.** Pictorial sketch of the *OPP* geometry.
- **Figure 2.** Pictorial sketch of the “candidate” building walls. $\{\tau_w^{(s)}; w = 1, \dots, W^{(s)}\}$, for the installation of *EMSs* to improve the *QoS* within the s -th ($s = 1, \dots, S$) *RoI*, $\Omega^{(s)}$.
- **Figure 3.** Block diagram of the *SbD*-based approach to the *EMSs* planning.
- **Figure 4.** Pictorial sketch of the local coordinate system for the (w, s) -th ($w = 1, \dots, W^{(s)}; s = 1, \dots, S$) *EMS*, $\Gamma_w^{(s)}$.
- **Figure 5.** *Numerical Assessment* - Picture of (a) the Google Map of the test-bed region (Gardolo district - Trento, Italy), (b) the corresponding cartography from the *OSM* database, and (c) the WinProp simulation scenario.
- **Figure 6.** *Numerical Assessment* ($f = 3.5$ [GHz], $L_y = 1.75$ [λ], $L_z = 7$ [λ]) - Model of the planar array of dual-polarization (slant-45) slot-coupled patch antennas along with the *HFSS* full-wave simulated co-polar gain pattern $G_{+45}(\theta, \phi)$.
- **Figure 7.** *Numerical Assessment* ($f = 3.5$ [GHz], $\mathcal{P}_{th} = -65$ [dBm], $S = 2$, $K = 20$) - Picture of (a) the reference/nominal received power distribution, $\mathcal{P}_0(\mathbf{r})$, and of (b) the corresponding thresholded power map.
- **Figure 8.** *Numerical Assessment* ($f = 3.5$ [GHz], $\mathcal{P}_{th} = -65$ [dBm], $S = 2$, $K = 20$) - Picture of (a)(b) the thresholded power map for the *Nominal Scenario* (i.e., w/o *EMSs*) and of (c)(d) the admissible locations for the *EMSs* deployment in the neighborhood of (a)(c) the *RoI* $\Omega^{(1)}, \Pi^{(1)}$, and of (b)(d) the *RoI* $\Omega^{(2)}, \Pi^{(2)}$.
- **Figure 9.** *Numerical Assessment* ($f = 3.5$ [GHz], $\mathcal{P}_{th} = -65$ [dBm], $S = 2$, $K = 20$) - Picture of the map of (a)(b) the thresholded power distribution for the *SbD*-optimized *EMSs* deployment and of (c)(d) the power gap distribution in the neighborhood of (a)(c) the *RoI* $\Omega^{(1)}, \Pi^{(1)}$, and of (b)(d) the *RoI* $\Omega^{(2)}, \Pi^{(2)}$.

- **Figure 10.** *Numerical Assessment* ($f = 3.5$ [GHz], $\mathcal{P}_{th} = -65$ [dBm], $S = 2$, $K = 20$)
- Plot of the *CDF* of the received power, $\Theta \left\{ \mathcal{P}(\mathbf{r}) | \hat{\mathcal{P}} \right\}$, within a circular region centered on the *RoI* $\Omega^{(1)}$, $\mathbf{r}_{\Omega}^{(1)}$, of radius $\zeta = 40$ [m].
- **Figure 11.** *Numerical Assessment* ($f = 3.5$ [GHz], $\mathcal{P}_{th} = -65$ [dBm], $S = 2$, $K = 20$)
- Picture of the thresholded power map in the neighborhood of the *RoI* $\Omega^{(1)}$, $\Pi^{(1)}$, when deploying (a) $Q^{(1)} = 1$ and (b) $Q^{(1)} = 2$ *EMSs* according to the *SbD*-based planning method.
- **Figure 12.** *Numerical Assessment* ($f = 3.5$ [GHz], $\mathcal{P}_{th} = -65$ [dBm], $S = 2$, $K = 20$)
- Plot of the *CDF* of the received power, $\Theta \left\{ \mathcal{P}(\mathbf{r}) | \hat{\mathcal{P}} \right\}$, within a circular region centered on the *RoI* $\Omega^{(2)}$, $\mathbf{r}_{\Omega}^{(2)}$, of radius $\zeta = 40$ [m].
- **Figure 13.** *Numerical Assessment* ($f = 3.5$ [GHz], $\mathcal{P}_{th} = -65$ [dBm], $S = 2$, $K = 20$)
- Picture of the thresholded power map in the neighborhood of the *RoI* $\Omega^{(2)}$, $\Pi^{(2)}$, when deploying (a) $Q^{(2)} = 1$, (b) $Q^{(2)} = 2$, and (c) $Q^{(2)} = 3$ *EMSs* according to the *SbD*-based planning method.
- **Figure 14.** *Numerical Assessment* ($f = 3.5$ [GHz], $\mathcal{P}_{th} = -60$ [dBm], $S = 4$, $K = 38$)
- Picture of the thresholded power map for the *Nominal Scenario* (i.e., w/o *EMSs*).
- **Figure 15.** *Numerical Assessment* ($f = 3.5$ [GHz], $\mathcal{P}_{th} = -60$ [dBm], $S = 4$, $K = 38$) -
Sketch of the admissible locations for the *EMSs* deployment in the neighborhood of (a)(c) the *RoI* $\Omega^{(3)}$, $\Pi^{(3)}$, and of (b)(d) the *RoI* $\Omega^{(4)}$, $\Pi^{(4)}$.
- **Figure 16.** *Numerical Assessment* ($f = 3.5$ [GHz], $\mathcal{P}_{th} = -60$ [dBm], $S = 4$, $K = 38$) -
Picture of (a)(b)(d)(e)(g)(h)(l)(m) the thresholded power map for (a)(d)(g)(l) the *Nominal Scenario* (i.e., w/o *EMSs*) and (b)(e)(h)(m) the scenario with the *SbD*-optimize *EMSs* along with (c)(f)(i)(n) the power gap distributions in the neighborhood of (a)-(c) the *RoI* $\Omega^{(1)}$, $\Pi^{(1)}$, (d)-(f) the *RoI* $\Omega^{(2)}$, $\Pi^{(2)}$, (g)-(i) the *RoI* $\Omega^{(3)}$, $\Pi^{(3)}$, and (l)-(n) the *RoI* $\Omega^{(4)}$, $\Pi^{(4)}$.
- **Figure 17.** *Numerical Assessment* ($f = 3.5$ [GHz], $\mathcal{P}_{th} = -60$ [dBm], $S = 4$, $K = 38$) -
Plot of the *CDF* of the received power, $\Theta \left\{ \mathcal{P}(\mathbf{r}) | \hat{\mathcal{P}} \right\}$, within a circular region of radius

$\zeta = 40$ [m] centered on (a) the *RoI* $\Omega^{(1)}$, $\mathbf{r}_{\Omega}^{(1)}$, (b) the *RoI* $\Omega^{(2)}$, $\mathbf{r}_{\Omega}^{(2)}$, (c) the *RoI* $\Omega^{(3)}$, $\mathbf{r}_{\Omega}^{(3)}$, and (d) the *RoI* $\Omega^{(4)}$, $\mathbf{r}_{\Omega}^{(4)}$.

TABLE CAPTIONS

- **Table I.** Descriptors of the urban scenario and of the *OPP*.

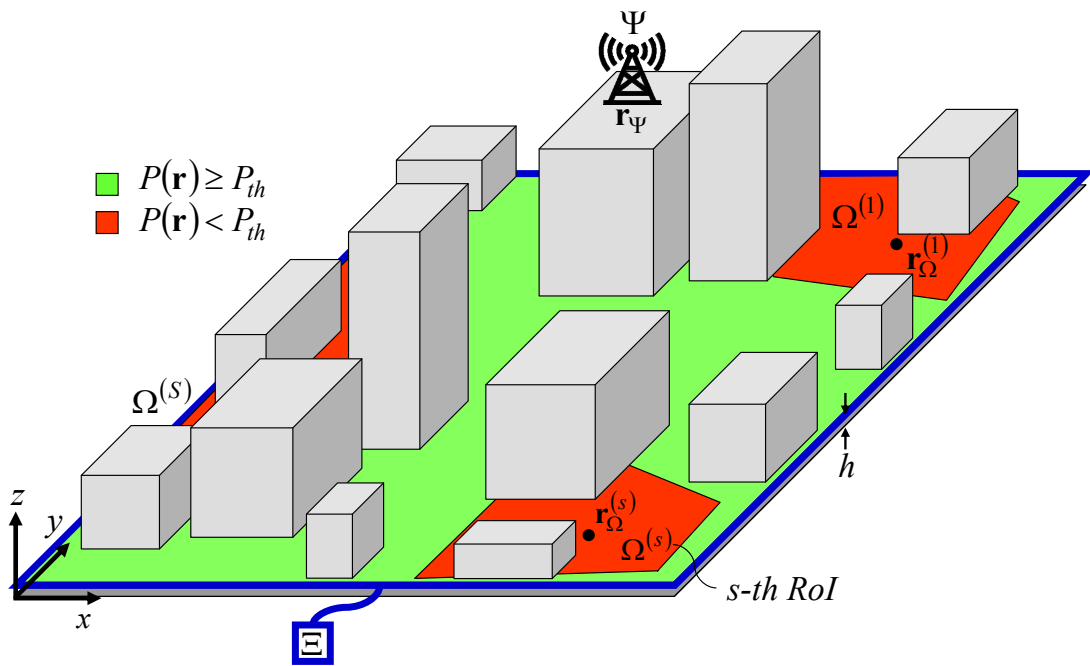


Fig. 1 - A. Benoni *et al.*, “Planning of EM Skins for ...”

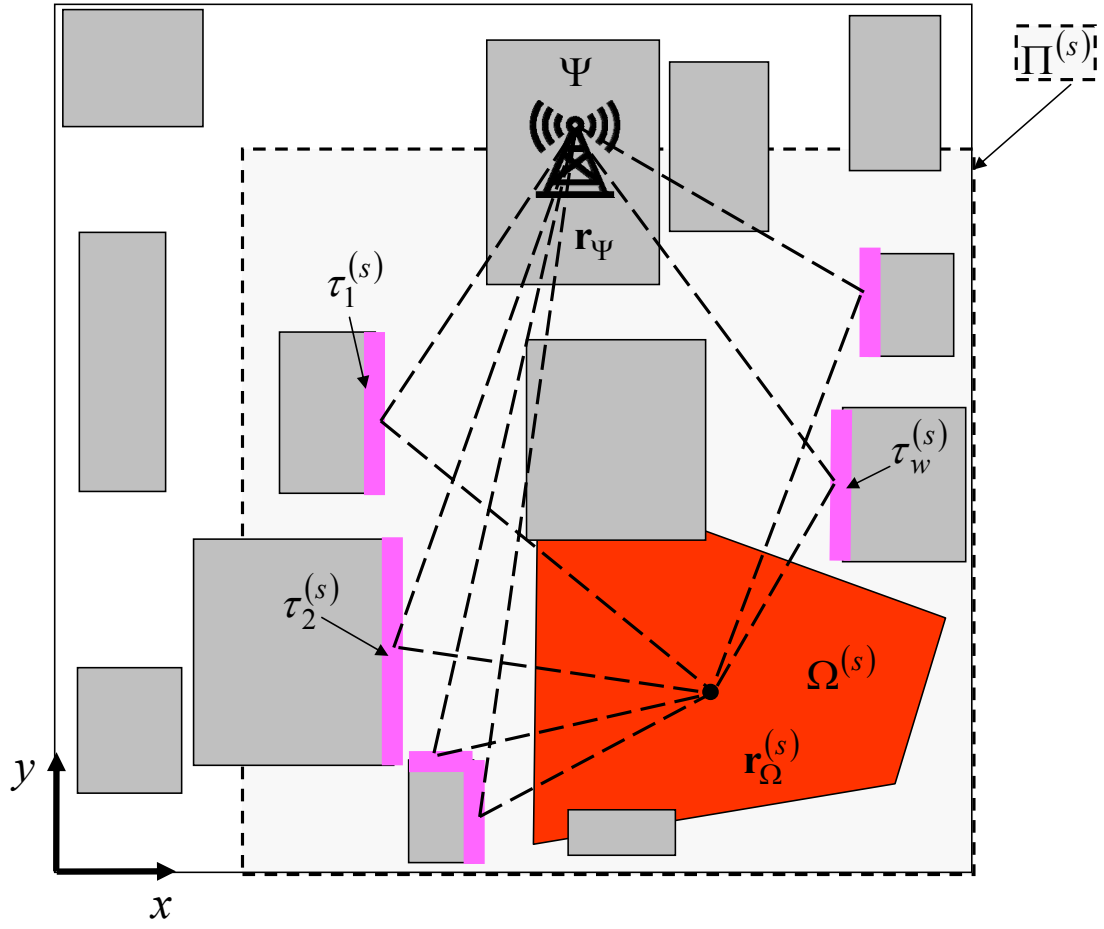


Fig. 2 - A. Benoni *et al.*, “Planning of EM Skins for ...”

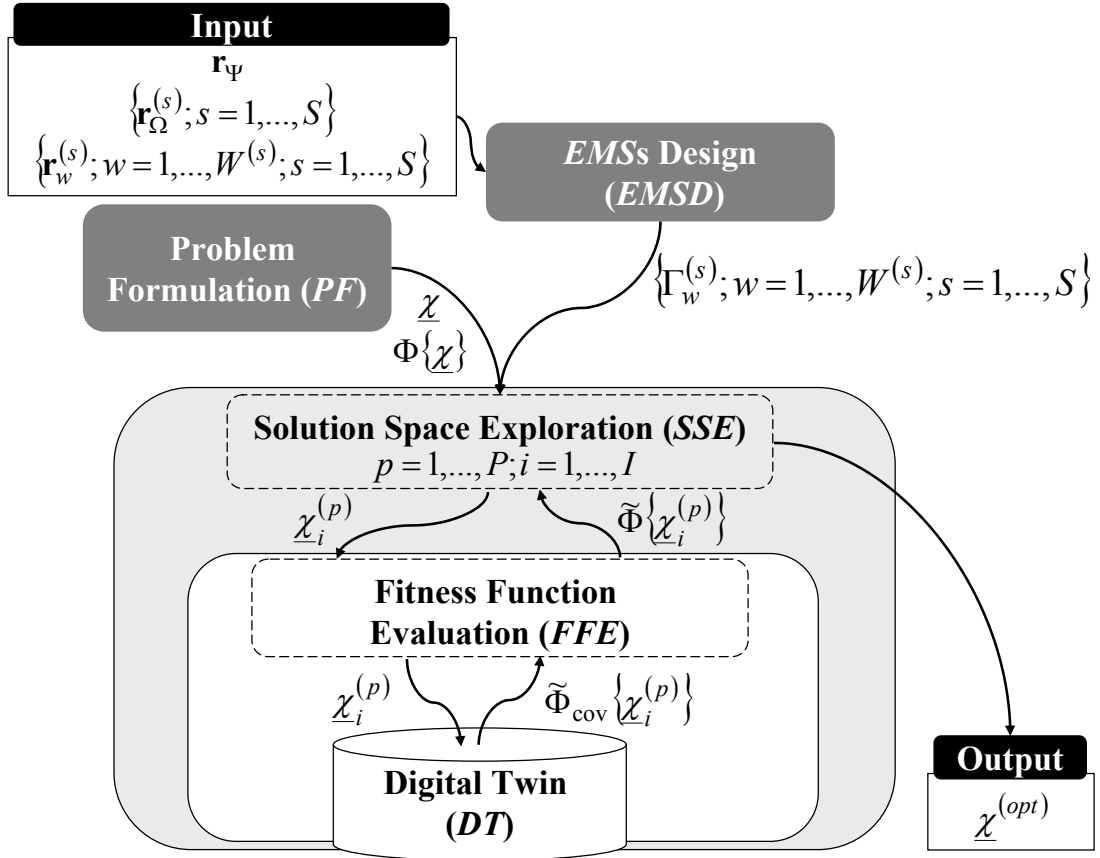


Fig. 3 - A. Benoni *et al.*, “Planning of EM Skins for ...”

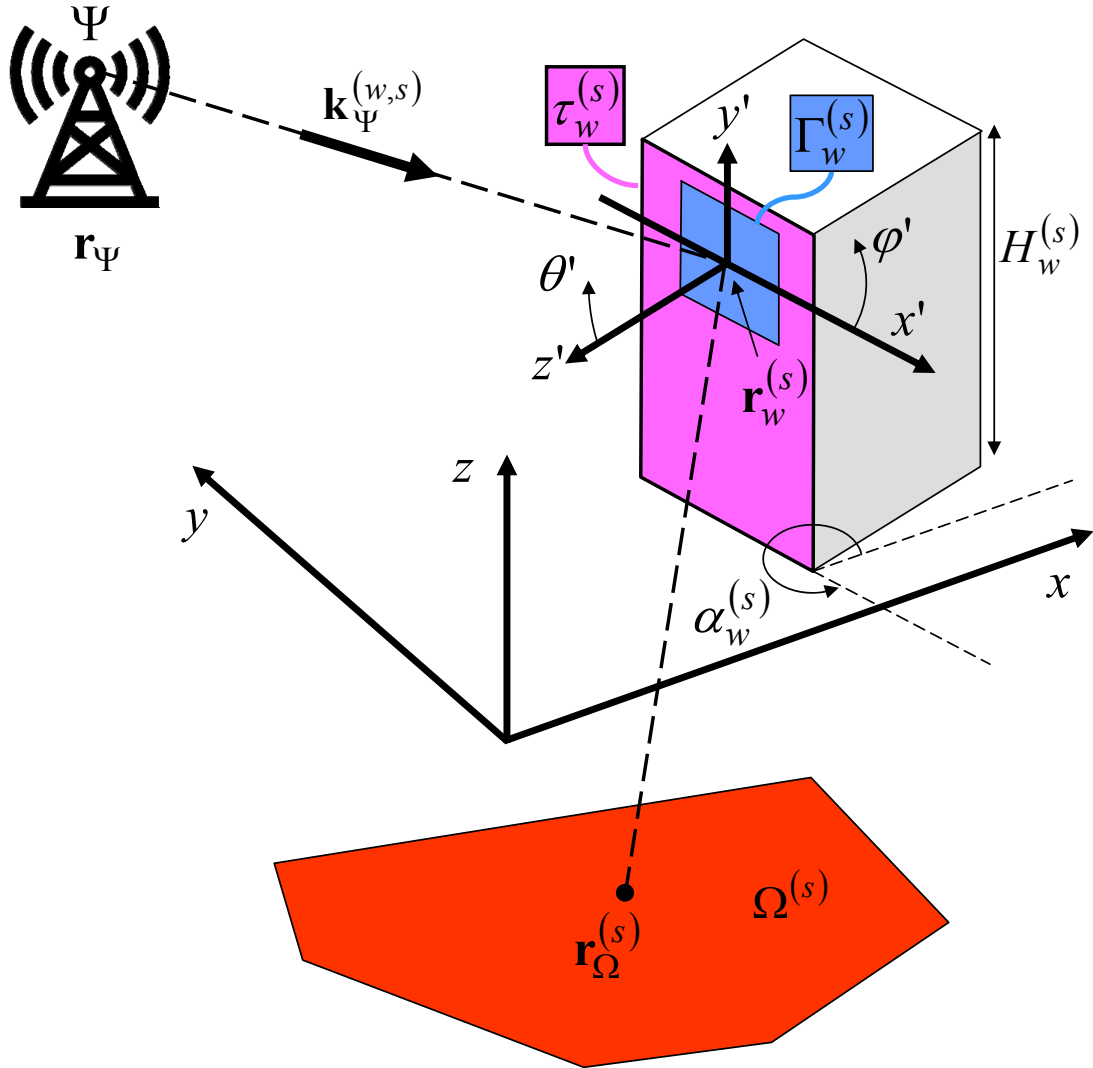
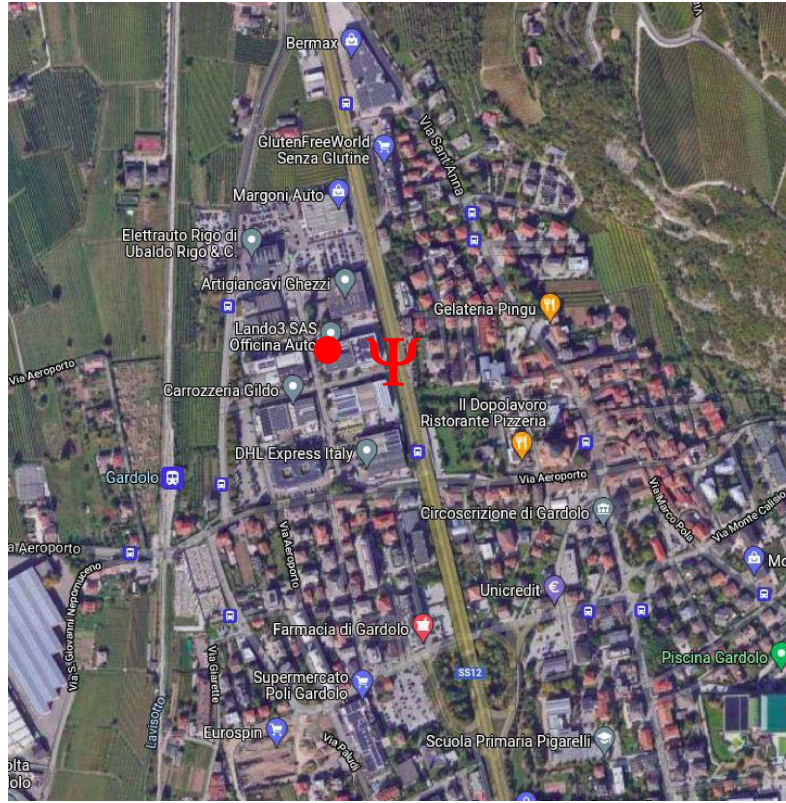
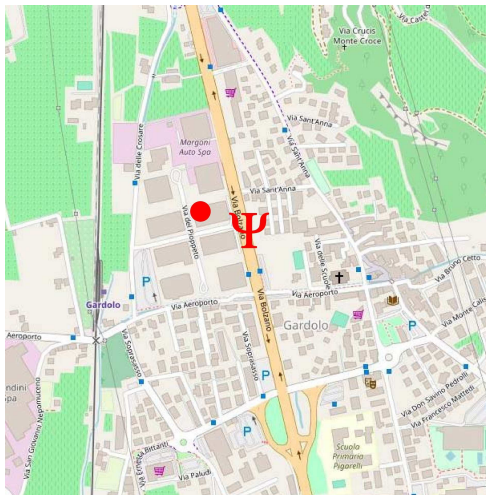


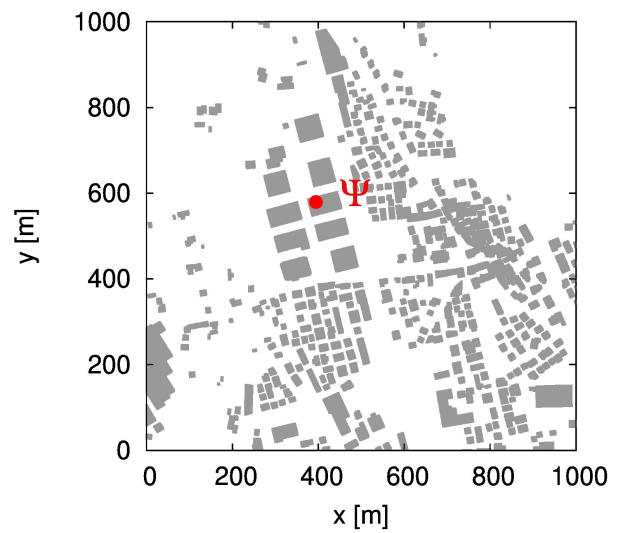
Fig. 4 - A. Benoni *et al.*, “Planning of *EM* Skins for ...”



(a)



(b)



(c)

Fig. 5 - A. Benoni *et al.*, “Planning of EM Skins for ...”

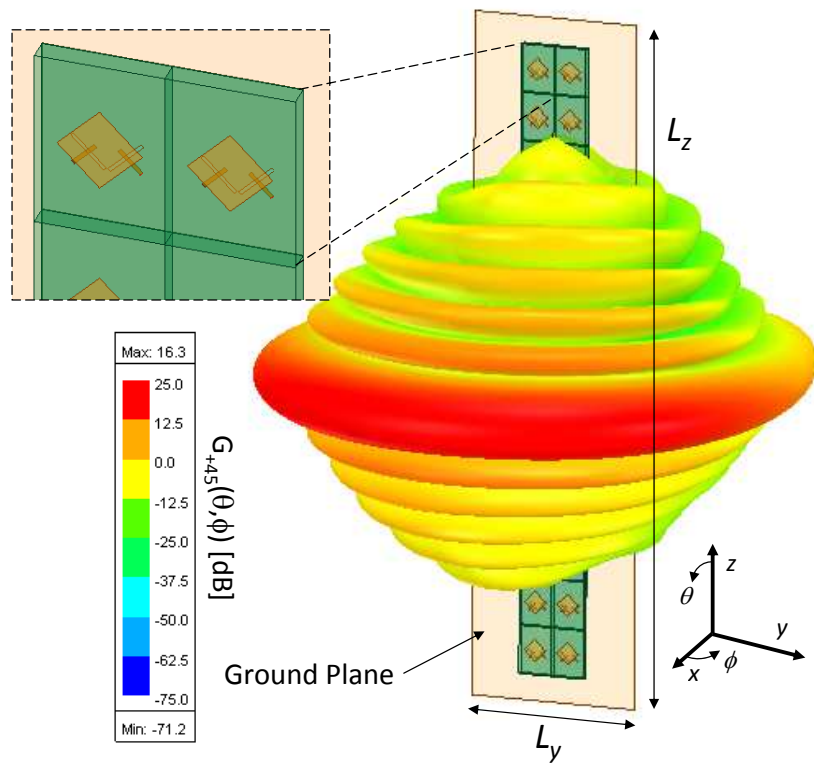
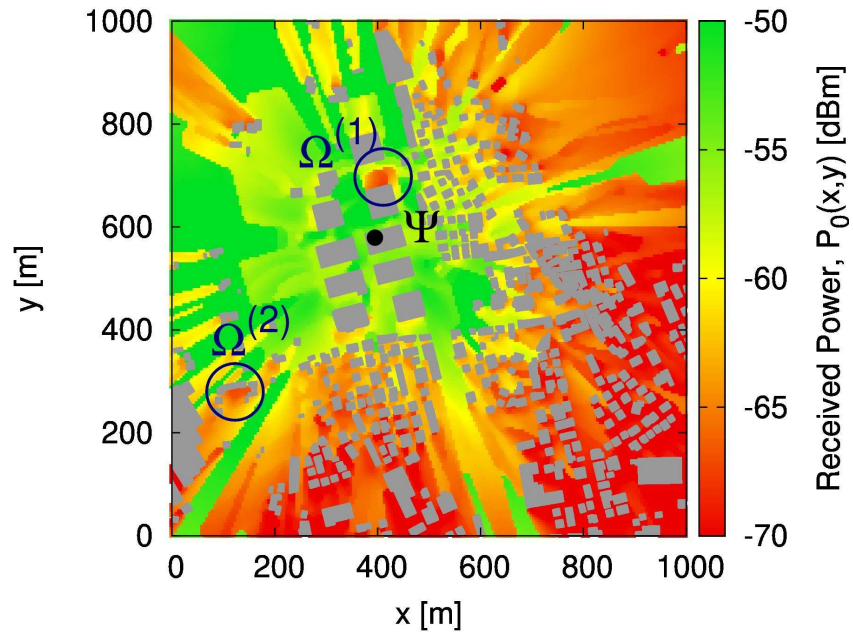
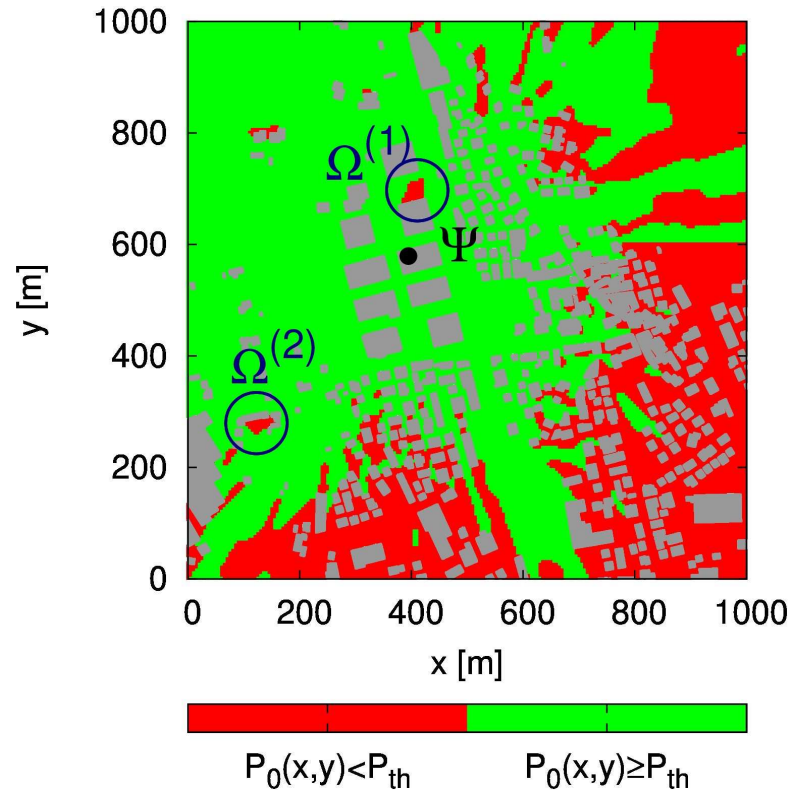


Fig. 6 - A. Benoni *et al.*, “Planning of EM Skins for ...”



(a)



(b)

Fig. 7 - A. Benoni *et al.*, “Planning of EM Skins for ...”

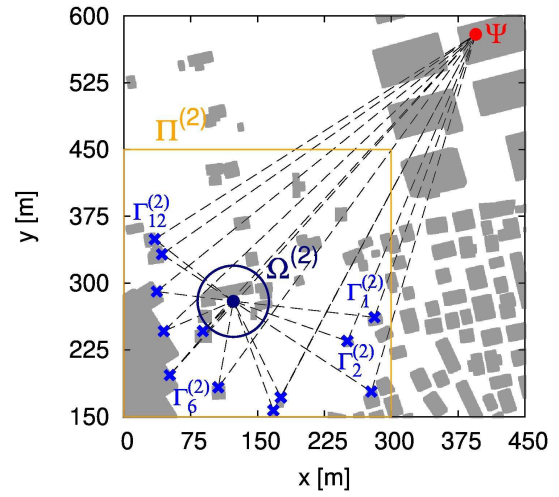
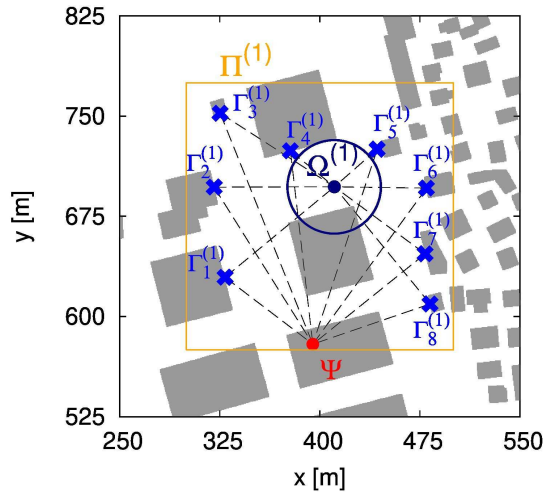
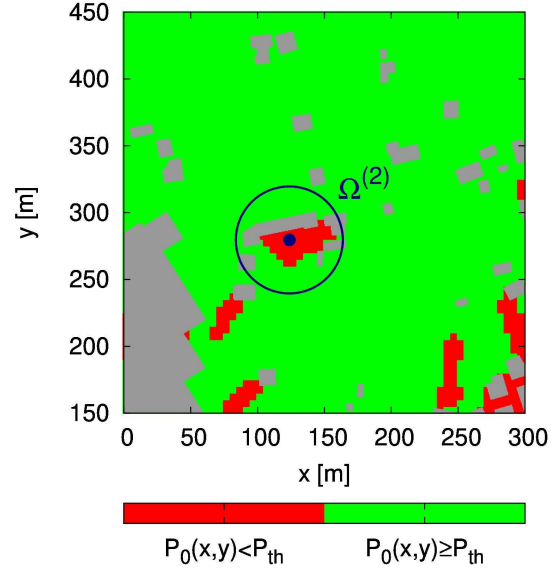
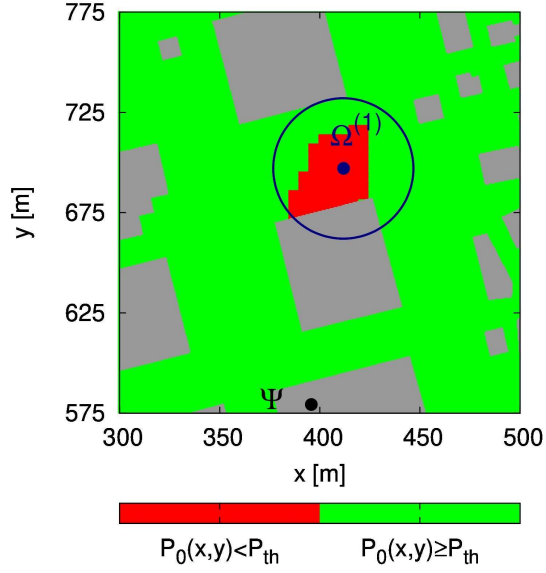


Fig. 8 - A. Benoni *et al.*, “Planning of EM Skins for ...”

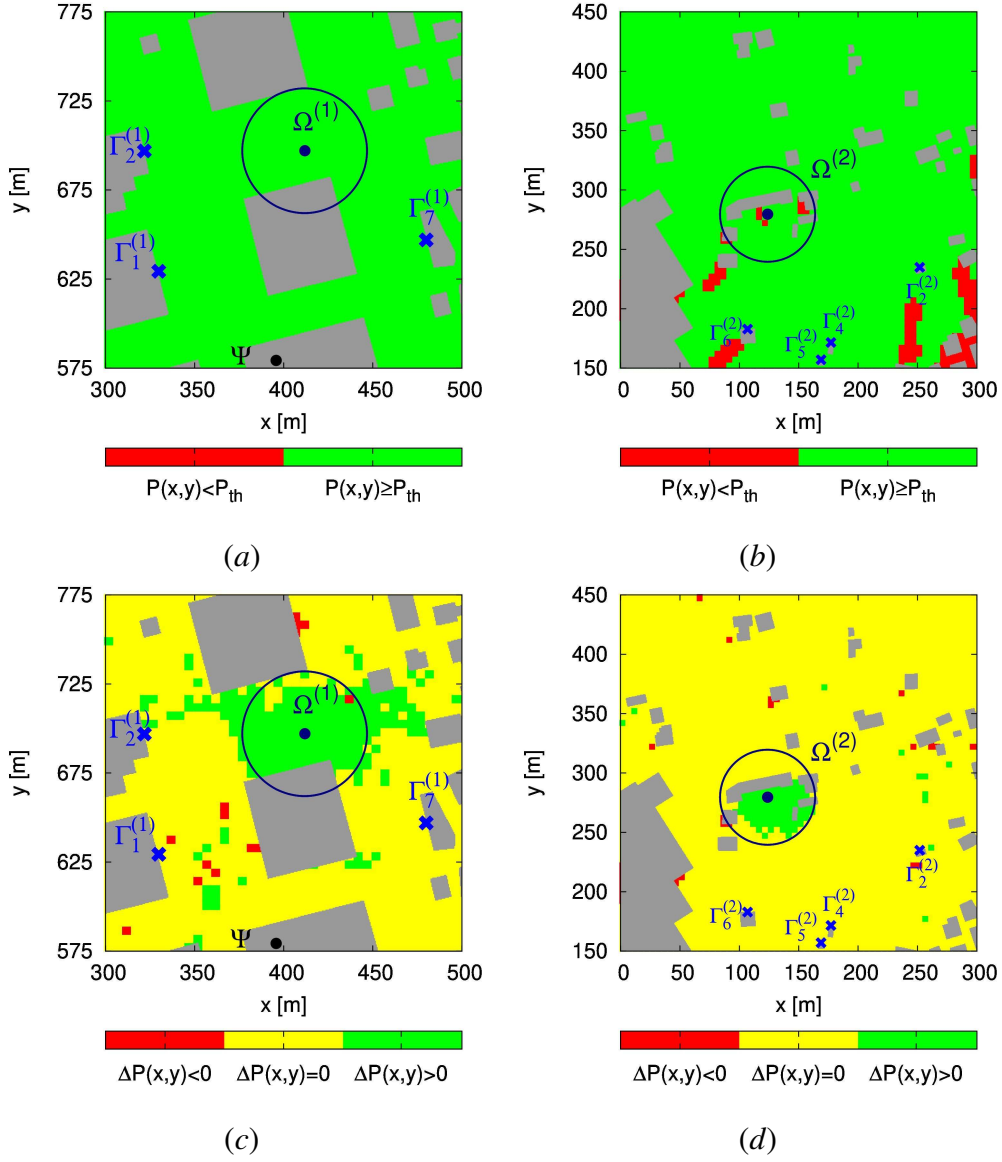


Fig. 9 - A. Benoni *et al.*, “Planning of EM Skins for ...”

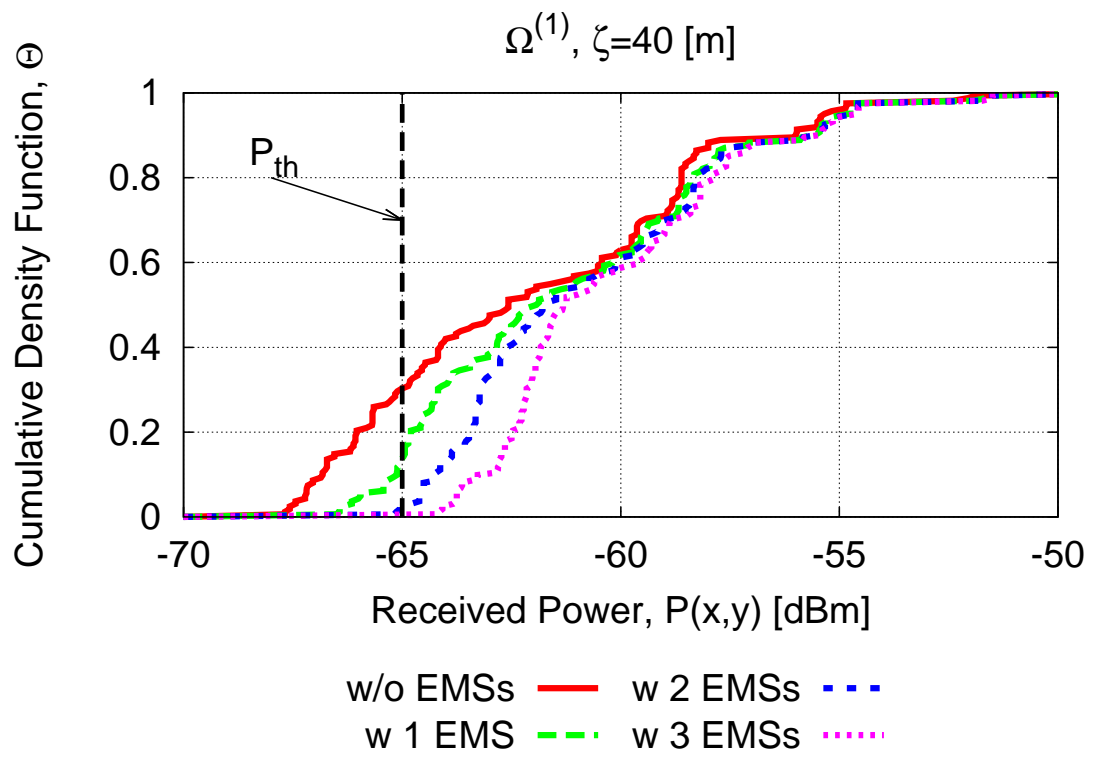


Fig. 10 - A. Benoni *et al.*, “Planning of *EM* Skins for ...”

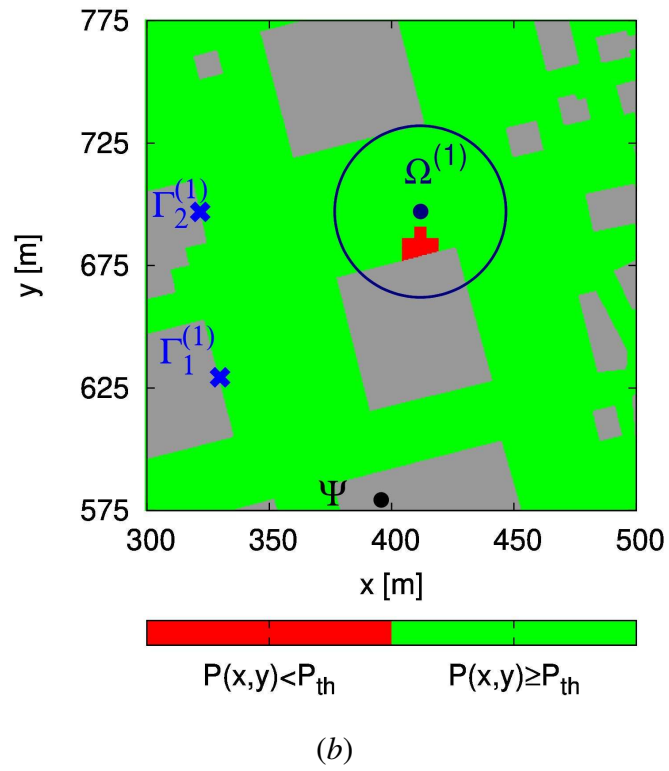
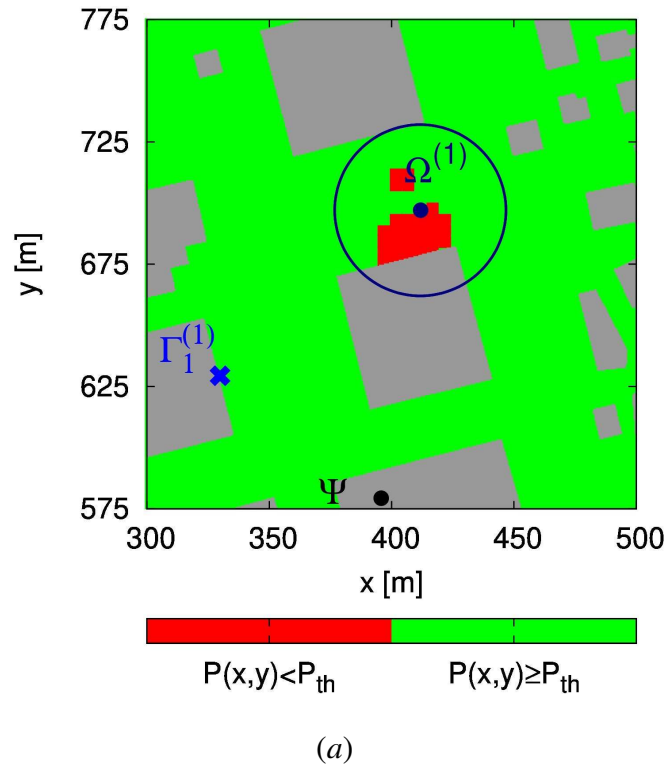


Fig. 11 - A. Benoni *et al.*, “Planning of *EM* Skins for ...”

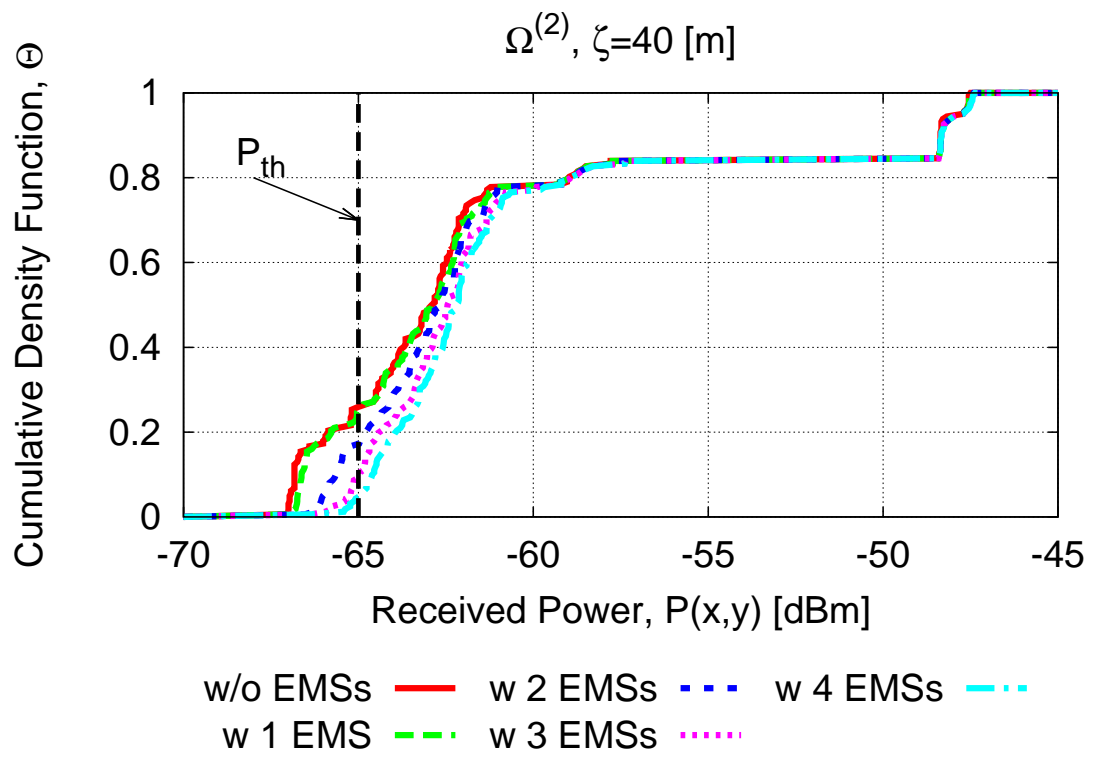


Fig. 12 - A. Benoni *et al.*, “Planning of *EM* Skins for ...”

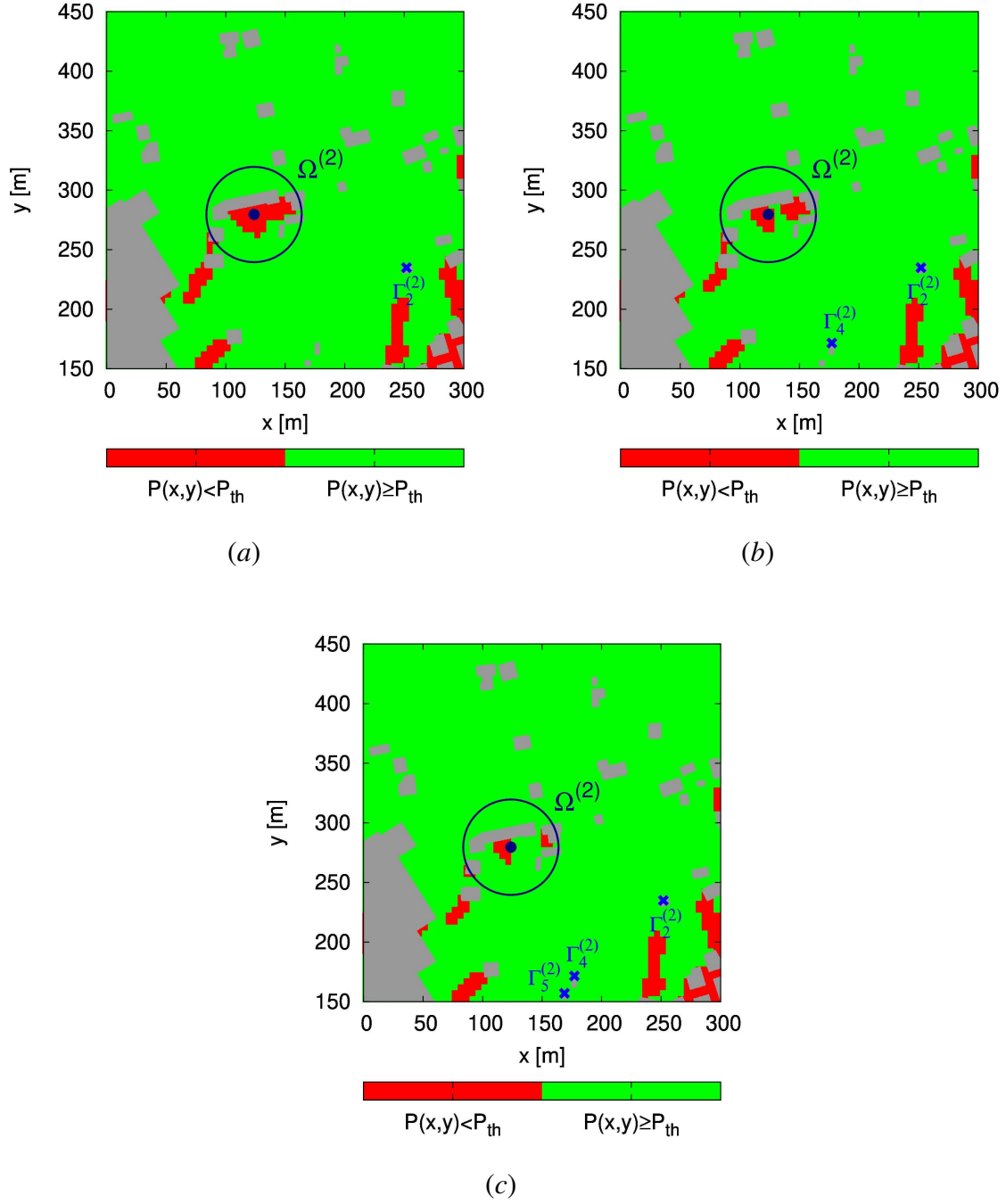


Fig. 13 - A. Benoni *et al.*, “Planning of *EM* Skins for ...”

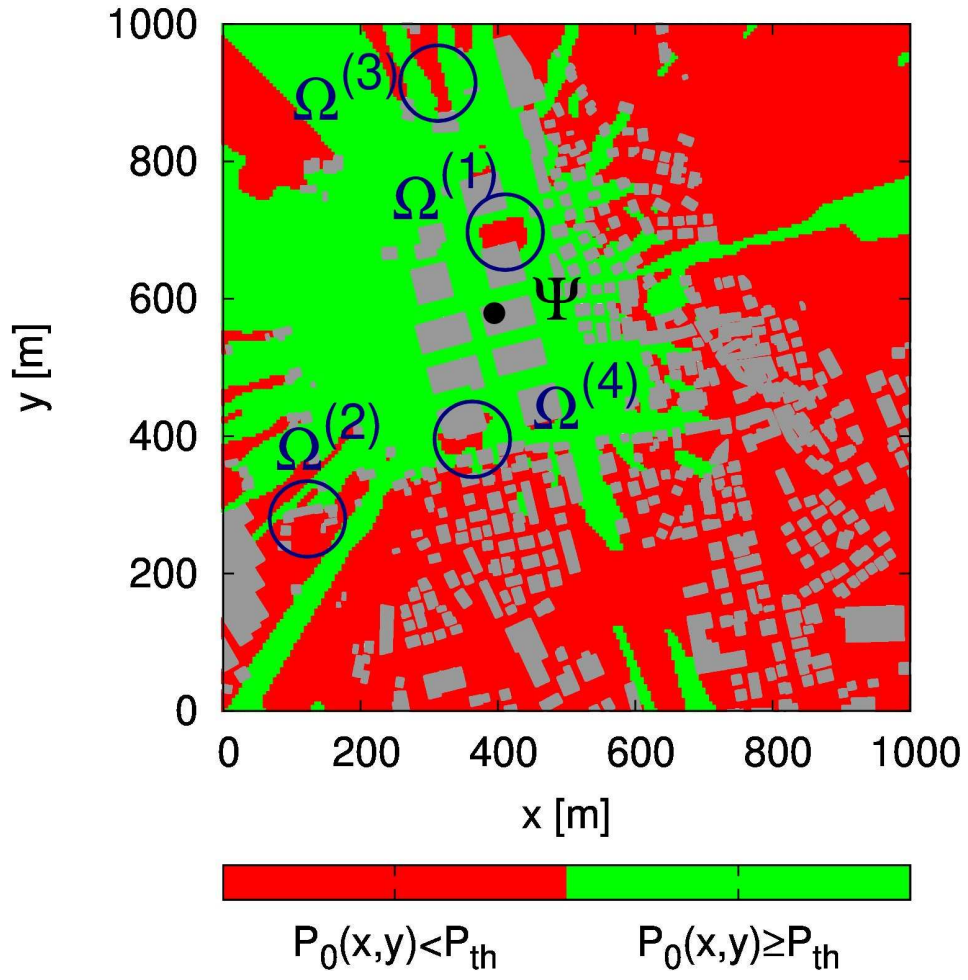
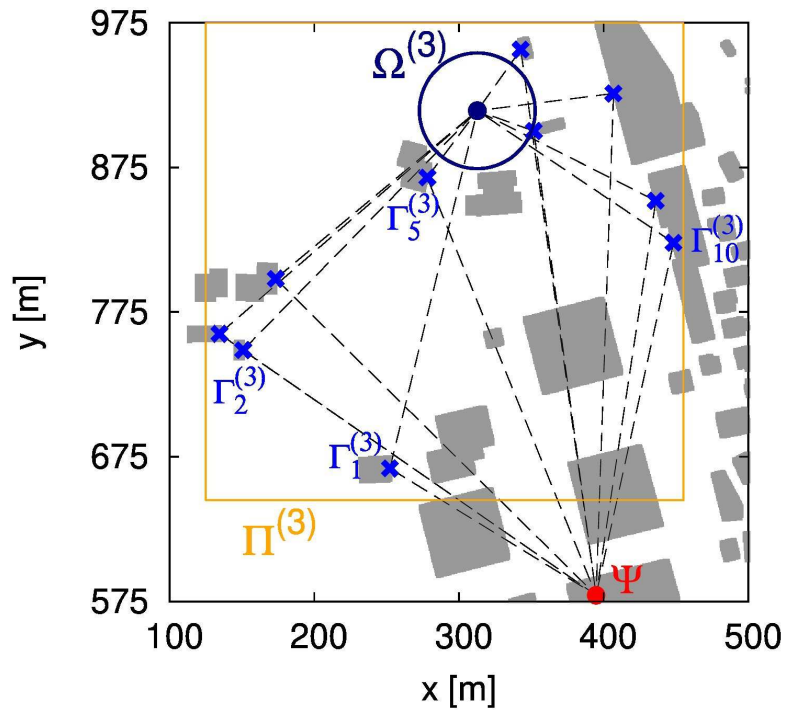
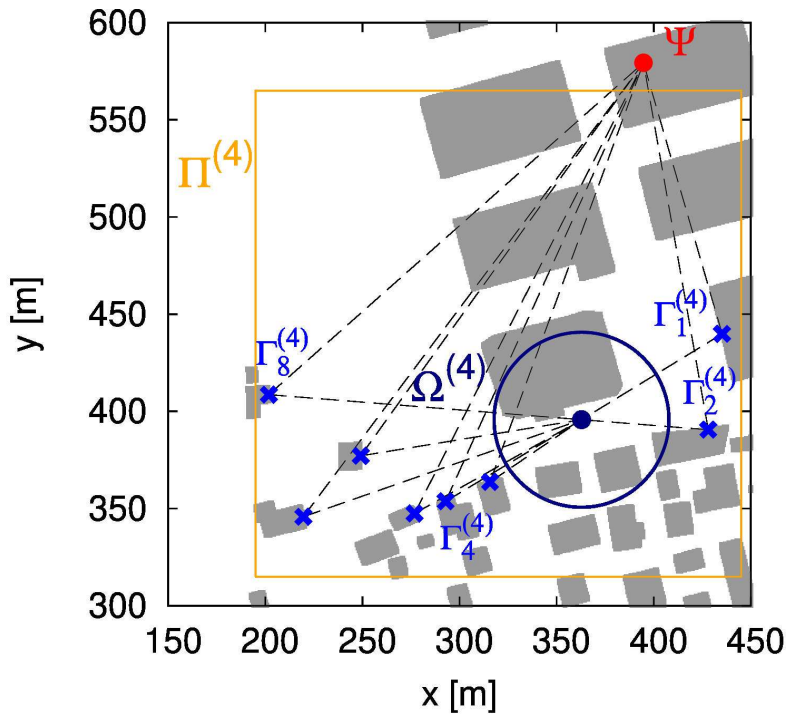


Fig. 14 - A. Benoni *et al.*, “Planning of *EM* Skins for ...”



(a)



(b)

Fig. 15 - A. Benoni *et al.*, “Planning of *EM* Skins for ...”

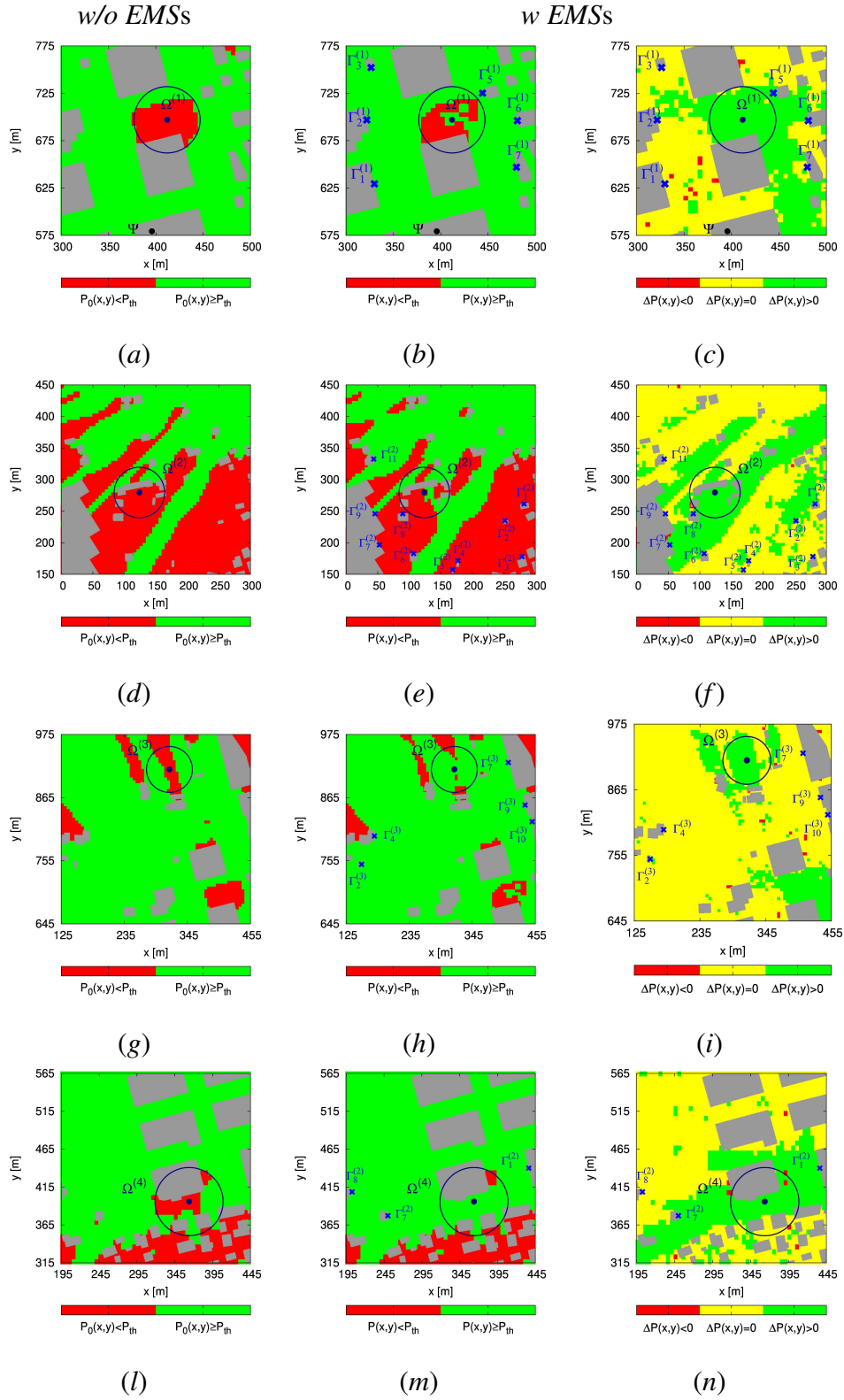
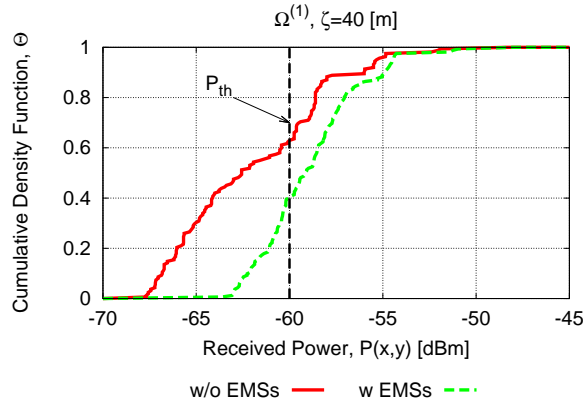
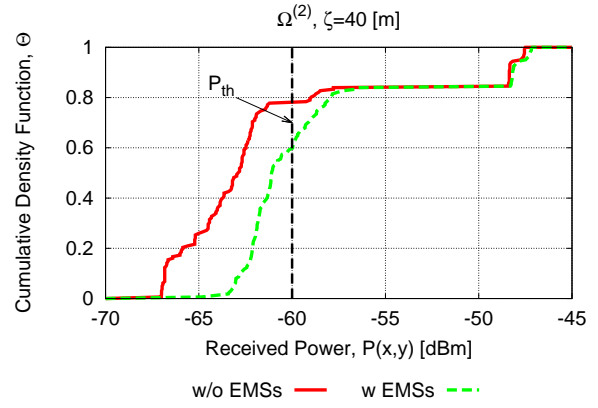


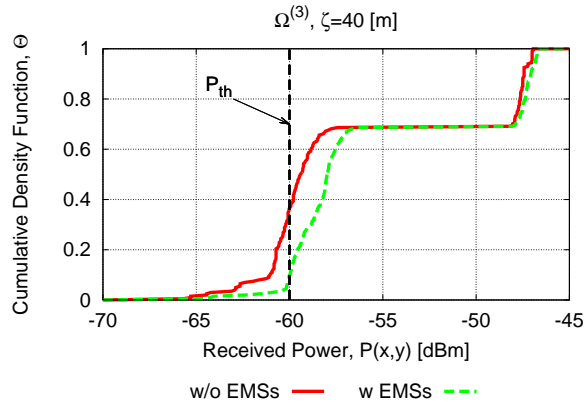
Fig. 16 - A. Benoni *et al.*, “Planning of EM Skins for ...”



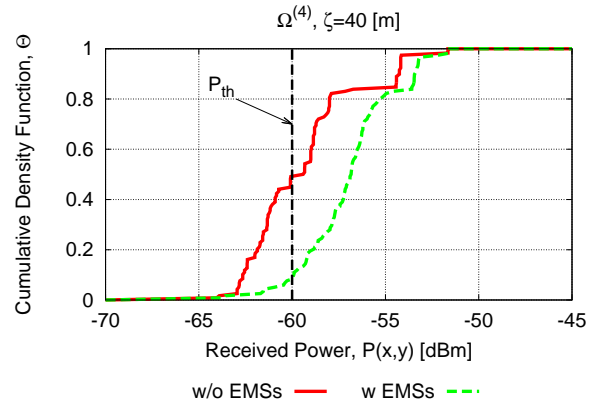
(a)



(b)



(c)



(d)

Fig. 17 - A. Benoni *et al.*, “Planning of EM Skins for ...”

\mathcal{P}_{th} [dBm]	S	K	B	$\Phi_{cov} \{\underline{\chi} = \underline{0}\}$	$Q^{(opt)}$	$\Phi \{\underline{\chi}^{(opt)}\}$	$\Phi_{cov} \{\underline{\chi}^{(opt)}\}$	$\Phi_{cost} \{\underline{\chi}^{(opt)}\}$
-65	2	20	1.05×10^6	2.10×10^{-2}	7	3.50×10^{-1}	2.50×10^{-4}	3.50×10^{-1}
-60	4	38	2.75×10^{11}	5.41×10^{-2}	24	6.46×10^{-1}	1.40×10^{-2}	6.32×10^{-1}

Tab. I - A. Benoni *et al.*, “Planning of *EM* Skins for ...”